NASA
Technical Memorandum 4248
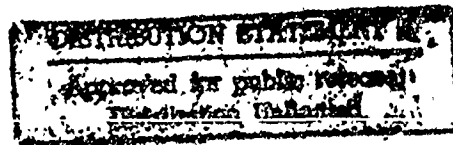
AVSCOM
Technical Report 90-B-010

AD-A230 876

Aerodynamic Effect of Strakes on Two-Dimensional Tail Boom Models of OH-58A and OH-58D Helicopters

Cynthia A. Crowell and Henry L. Kelley

DECEMBER 1990

NASA

US ARMY
AVIATION
SYSTEMS COMMAND
AVIATION R&T ACTIVITY

Aerodynamic Effect of Strakes on Two-Dimensional Tail Boom Models of OH-58A and OH-58D Helicopters

Cynthia A. Crowell and Henry L. Kelley
Aerostructures Directorate
USAARTA-AVSCOM
Langley Research Center
Hampton, Virginia

Summary

During hover and low-speed flight, helicopters experience significant aerodynamic forces on the tail boom caused by the wake from the main and tail rotors and by crosswinds. These effects were investigated in the Langley 14- by 22-Foot Subsonic Tunnel on 136-percent-scale two-dimensional tail boom models with cross sections representative of those on the U.S. Army OH-58A and the OH-58D helicopters. The effects of longitudinal strakes attached to the cross sections were also investigated. The aerodynamic forces acting on the cross sections were obtained by varying flow incidence on the scaled models from $-45°$ to $90°$ and dynamic pressure from 5 to 15 psf.

The results indicate a significant improvement at conditions which represent right sideward flight by reducing the adverse aerodynamic side force when the strakes are installed. These data were used to calculate a change in tail rotor power for the full-scale flight vehicle and indicated approximately a 5- to 6-percent average savings in right sideward flight for the critical velocity range of 0 to 30 knots. Of course, an increase in the tail boom download was noted because of the strakes. The results indicate a potential for reducing the directional control and tail rotor thrust required in the critical hover and right sideward flight speed range with a calculated minimum increase in main rotor power required and an overall net improvement in power of about 0.5 percent for both the OH-58A and OH-58D.

Introduction

A helicopter is subjected to complex airflows that are self-imposed as a result of the main and tail rotor wakes and as a result of ambient wind. These airflows produce aerodynamic forces on the fuselage and tail boom assembly during hover and low-speed sideward flight (refs. 1 and 2). When operating in this portion of the flight envelope, the airflow from the main rotor wake has a large impact on the tail boom forces. These effects cause the tail boom to be subjected to air loads which must be counteracted by main rotor and tail rotor thrust to maintain aircraft trim. These increased power requirements result in a reduction in payload and yaw control margin.

Until recently, studies of blunt-body shapes have been applicable to fixed-wing aircraft. Although this study indicated the aerodynamic sensitivity of these shapes to Reynolds number and incidence angle, none have included cross sections that resemble those of typical helicopter tail booms with a drive-shaft cover nor considered the unique air load characteristics these shapes would produce (refs. 3 through

8). Over the past several years, in an effort to reduce the adverse boom forces and moments, wind tunnel and flight studies have been made to determine the effect of several tail boom strake configurations for models of the UH-1H, AH-64, and UH-60 (ref. 9). Results from these tests have shown a potential for the use of strakes to reduce tail rotor thrust and improve yaw control margin in right sideward flight. In right sideward flight, before the main rotor downwash clears the tail boom, the demand for tail rotor thrust is increased as airspeed increases. In left sideward flight, the tail rotor thrust requirement decreases as airspeed increases. Tests were made at flow angles that were representative of left and right sideward flight conditions to ensure there were no adverse effects in left sideward flight and to analyze the benefit the strakes would have in right sideward flight (refs. 10 through 12).

In order to document these effects, an investigation was made in the Langley 14- by 22-Foot Subsonic Tunnel with 136-percent-scale cross sections of circular-shaped tail booms with drive-shaft covers representative of the U.S. Army OH-58A and the OH-58D helicopters (fig. 1). Strakes were applied longitudinally at selected angular locations to all models to determine their effectiveness in changing the side forces and normal forces acting on the tail boom. A 2-inch upper strake and a 1-inch lower strake were applied to the model at various locations shown in table I and figure 2. Aerodynamic forces and moments resulting from the airflow around the tail boom cross sections in the various configurations were measured over a range of dynamic pressure from 5 to 15 psf and over a range of flow incidence from $-45°$ to $90°$. The results are presented as plots of boom normal-force and side-force coefficients as functions of flow incidence and dynamic pressure for each configuration. An increased normal force (boom download) is compensated for by a required increase in main rotor thrust and required power. A positive side-force coefficient increment results in an increase in tail rotor power required. In addition, calculations were made to equate the force changes to changes in tail rotor power and main rotor power for the full-scale helicopters.

Symbols

The aerodynamic data convention and angle of flow incidence are shown in figure 1.

BL   baseline model

b maximum width of cylinder normal to flow at zero flow angle, ft

b_1 maximum width of aircraft tail boom at point that lies at 80 percent of main rotor radius, ft

c maximum depth of cylinder parallel to flow at zero flow angle, ft

c_y section side-force coefficient, $\dfrac{\text{Side force per unit length}}{bq}$

c_z section normal-force coefficient, $\dfrac{\text{Normal force per unit length}}{bq}$

D_1 length of tail boom, ft

D_2 distance from aircraft center of gravity to point on tail boom that lies at 80 percent of main rotor radius, ft

D_3 distance from aircraft center of gravity to tail rotor center of rotation, ft

F_N aircraft normal force, lb

F_Y aircraft side force, lb

$L_{P,mr}$ assumed main rotor power loading, 8 lb/hp

$L_{P,tr}$ assumed tail rotor power loading, 4 lb/hp

q tunnel dynamic pressure, $\frac{1}{2}\rho V^2$, psf

R Reynolds number, $\dfrac{\rho V c}{\mu}$

S calculated tail boom reference area, ft^2

S_x configuration identification, see table I

V free-stream velocity in tunnel, ft/sec

v sideward velocity of helicopter, knots

v_s velocity of slipstream in rotor wake, ft/sec

μ viscosity, slugs/ft-sec

ρ free-stream air density, slugs/ft^3

ϕ angle of flow incidence in plane normal to axis of two-dimensional cylinder, deg

Model and Apparatus

Two models with cross-sectional shapes representative of tail booms of U.S. Army OH-58A and OH-58D helicopters were tested. A circular cylinder model was also tested which represented a tail boom without a drive shaft cover. The cross-section shapes were a 136-percent scale of the full-scale tail booms. These shapes represent a section of the boom located at a point 80 percent of the main rotor radius aft of the main rotor mast centerline. This is the area under the main rotor in which near maximum rotor wake velocities are experienced in hover (ref. 9). Sketches of the models are shown in figure 3. Each model had the same diameter of 15 in. The full-scale boom diameters are 11 in. at 80 percent of the rotor radius. The drive-shaft cover for the OH-58A is 19 percent smaller in width and 31 percent smaller in height than the drive-shaft cover for the OH-58D.

The models were constructed of aluminum sheet metal attached to aluminum bulkheads with flush screws. The surfaces were smooth and did not have the customary protruding rivetheads characteristic of OH-58 helicopter tail booms. Longitudinal strakes were used on the models in several configurations varying the height of the strake and angular placement of the strake around the boom (fig. 2). These configurations were based on analysis of past results from tail boom model tests (ref. 9).

The installation of the model in the Langley 14-by 22-Foot Subsonic Tunnel is shown in figure 4. A sketch of the components and the balance is shown in figure 5. The model was constructed in three major sections. The upper and lower sections of the model were rigidly fixed to a strut that ran through the center of the model. The middle section was attached to a strain-gauge balance that measured the forces and moments. The other end of the balance was attached to the center strut. The strut extended through the floor of the tunnel to a model mounting support which allowed the model to be rotated about the vertical axis to vary flow incidence. Large circular plates (48 in. in diameter) were placed at both ends of the model to ensure that evenly distributed two-dimensional flow would occur on the metric section of the model.

Tests

Data were taken at a constant tunnel dynamic pressure for each run while the model was rotated through the range of flow incidence of $-45°$ to $90°$. Data were taken every $5°$ of incidence from $-25°$ to $30°$ and every $10°$ from $-45°$ to $-25°$ and $30°$ to $90°$. These angles represent the change in airflow angle over the tail boom due to various sideward flight speeds. Data were taken at $q = 5$, 10, and 15 psf. These values of q were selected to include those conditions that would encompass the Reynolds number range experienced by full-scale OH-58A and OH-58D helicopter tail booms. The dynamic pressures as a function of Reynolds number are shown in figure 6 for the cylinder and the OH-58A and OH-58D tail boom models. At $q = 15$ psf, for the cylinder model, $R = 0.87 \times 10^6$, for the OH-58A tail boom model,

$R = 1.19 \times 10^6$; and for the OH-58D tail boom model, $R = 1.30 \times 10^6$. Figure 7 shows the effects of an increase in q on c_z acting on the cylinder model. The six-component strain-gauge balance used in this test had an accuracy for both normal and side force of ± 1.25 lb; however, the general repeatability of the force measurements was approximately 0.20 lb. Data were taken at various dynamic pressures; however, the data shown in the report, other than figure 7, was taken at 15 psf. Accuracy at 15 psf was ± 0.03 for c_z and c_y with a repeatability of 0.009.

The maximum test Mach number was approximately 0.18; therefore, compressibility effects were considered to be negligible. Due to the small projected area of the test apparatus relative to the large test area, the data did not require correction for tunnel blockage effects (ref. 13).

Presentation of Data

The results are presented as normal-force coefficient c_z and side-force coefficient c_y. The coefficients are based on the dimension b, boom width, which is consistent with presentations of data presented in references 3 through 9.

Arrangement of data figures is as follows:

Discussion of Results

The desired results were an increase in the right side-force coefficient in the critical range $\phi = 0°$ to 45°. This is the approximate range in which helicopters initiate right sideward flight up through the point at which the main rotor downwash clears the tail boom. In addition, some of these data were used to compute what effect strakes would have on the performance of the full-scale aircraft. These results show the percentage of change in main rotor and tail rotor horsepower when comparing a nonstraked aircraft to a straked aircraft based on a fully loaded aircraft configuration. The increased normal force (boom download) is compensated by an increase in main rotor power. A positive increment in right side-force coefficient results in a decrease in tail rotor power required.

Based on previous results (ref. 9), consideration was given to several factors that have caused uncertainties in these kinds of tests in the past. The model surface was not polished, but unlike the actual aircraft skin, it had no rows of rivet heads. The sheet metal on the model was secured by sunken screws that were then taped over. Viscosity is one factor that has been shown to have a significant effect on the data (refs. 3 through 9). The actual aircraft experiences varying Reynolds numbers. In the Reynolds number range from 0.3×10^6 to 0.7×10^6, large changes can occur in the lift and drag forces on a model. Since the data were taken at higher Reynolds numbers of 0.97×10^6 to 1.30×10^6 (fig. 6), these large changes should not be a concern (refs. 3 and 4). A third factor is the hysteresis effect on the data caused by flow separation which alters the way in which the dynamic pressure or flow incidence is changed between data points. To determine the effects of changing the sequence of ϕ, several runs were made from $-45°$ to 90° and then from 90° to $-45°$. The test results are presented in figure 8 and show that there is relatively little difference in the data within the critical range $\phi = 0°$ to 45°.

Another opportunity to experience a hysteresis effect is during a dynamic pressure sweep. If, for

example, one run started at $q = 0$ psf and increased to the maximum q and the next run was conducted at the high end of q and then decreased to 0 psf, the repeatability of the data may be poor. This effect was avoided by starting all data runs at $q = 0$ psf. The final factor to be considered was turbulence in the tunnel test section. Because of improvements to the 14- by 22-Foot Subsonic Tunnel over the past few years, the intensity of turbulence is only 0.1 percent (ref. 14) and, therefore, was not a factor. A comprehensive technical description of the 14- by 22-Foot Subsonic Tunnel is given in reference 15.

Basic Configurations

The models used during this investigation represent cross sections of tail booms of the OH-58A and the OH-58D helicopters at a vertical section located aft of the main rotor mast at 80 percent of the rotor radius. A cylinder the size of these tail booms without the drive-shaft cover was also tested as a reference. The results of the cylinder would not reflect the same data as the OH-58A and OH-58D without their drive-shaft cover due to the exposed rotating drive-shaft and cover retaining devices that would alter the airflow. The coefficient c_y and c_z as a function of ϕ for these three models are shown in figure 9. In figure 9(a), the drive-shaft covers from both aircraft have relatively the same effect for $\phi = -20°$ to 40° for c_z. When compared with the cylinder, the influences of the drive-shaft covers are evident with the reduced c_z for $\phi = -25°$ to 50° and to 80° for the OH-58D model with drive-shaft cover on. This would mean a slight reduction in main rotor power to compensate for the reduction in normal force. There is also an increased negative value of c_y from $\phi = 0°$ to 90° (fig. 9(b)). This shift in c_y would burden the helicopter tail rotor in hover or right sideward flight by causing an unfavorable shift in the fuselage yawing moment and thereby increase the tail rotor power required to control aircraft heading.

Characteristics of Each Model

The side-force and normal-force coefficients as a function of ϕ obtained at a tunnel $q = 15$ psf are discussed for each model individually. The data at $q = 15$ psf are above the critical Reynolds number. Table I describes the strake configuration used on each of the shapes. Three different lower strake positions were selected to improve side force as well as reduce normal force (fig. 2). A benefit would be a positive increase in c_y over the baseline. This implies a change in side force to the right and in a direction to assist the tail rotor thrust. The tail rotor thrust required would decrease as a result of this shift in side

forces. The flow angles ϕ in which a positive increase in c_y is the most critical would be from 0° to 45°. This is the approximate range in which helicopters initiate right sideward flight up through the point at which the main rotor downwash clears the tail boom. The envelope of both right and left sideward flight flow incidence was studied to determine if there were any adverse effects for left sideward flight and to look at possible improvements in right sideward flight.

Cylinder

One of the most common two-dimensional shapes that has been tested is the circular cylinder. When comparing the results of the dynamic pressure sweep in figure 7 with the results of another test (fig. 9(b) of ref. 9), the outcome shows similar variations of c_z as a function of ϕ. When strakes were placed on the model, the influence was demonstrated as an increase in c_z in the critical range $\phi = 0°$ to 45° as shown in figures 10(a) and 11(a). Figures 10(b) and 11(b) show the effect of the strakes on c_y. The location of the strakes on the model affect the degree of improvement. Based on the effect on c_y, the least effective was configuration S_a with a strake placed 30° from the top of the cylinder and a second strake placed at 150° from the top of the cylinder. The most effective was configuration S_b with the strake at 60° from the top of the tail boom and another strake at 150° from the top of the tail boom. In figure 10(a) there is an increase in c_z from $\phi = -10°$ to 80° for configuration S_a compared with the baseline cylinder. Figure 11(a) shows the effect on c_z when the upper strake is the same and the lower strake position is changed. Configuration S_c initiates a downward trend at $\phi = 50°$, and S_d initiates a reduction at $\phi = 30°$. In figure 10(b) for configuration S_a the flow appears to reattach to the surface of the model based on the limited improvement of c_y when compared with configuration S_b. In comparing the three different positions for the lower strake, for c_y as a function of flow incidence (fig. 11(b)), the improved positive c_y no longer exists at $\phi = 50°$ for S_c and at $\phi = 35°$ for S_d. Configuration S_b shows an improvement in c_y throughout the test range of ϕ.

OH-58A Model Tail Boom Configuration

With the placement of a drive-shaft cover on the OH-58A model, a more diverse test matrix was studied. The upper strake was placed at 30° (fig. 12), and 60° (fig. 13) on the drive-shaft cover and at 60° (fig. 14) on the tail boom. The lower strake was in the same three locations of 150°, 180°, and 210° for each upper strake location. The results were compared with the baseline OH-58A model

without strakes. The range of ϕ in which a positive increase in c_y is most critical is from $\phi = 0°$ to $45°$, which is where the helicopter initiates right sideward flight up to the point at which the main rotor downwash clears the tail boom. The results from the baseline configuration and the upper strake location on the drive-shaft cover at $30°$ with the three variations to the lower strake are shown in figure 12. From $\phi = -40°$ to $10°$, the strake configurations make relatively no change to c_z (fig. 12(a)). From $\phi = 10°$ to $45°$, there is an increase in the normal-force coefficient for the three strake configurations. The results for c_y shown in figure 12(b) indicate a reduced side-force coefficient from $\phi = -10°$ to almost $15°$ with an increase from $\phi = 15°$ to $40°$ for all strake configurations. The results for the lower strake configuration placed at $210°$ indicate a reduced benefit in c_y compared with that for $150°$ and $180°$ for $\phi = 25°$ to $45°$. Though the strake placed on the drive-shaft cover at $30°$ offers an improvement from $\phi = 15°$ to $40°$, it is not a recommended solution due to an adverse reduction of c_y compared with the baseline from $\phi = 0°$ to $15°$.

In figure 13, where the results are shown for the configuration with the strakes placed at $60°$ on the drive-shaft cover, the effect is very similar to the strake configuration at $30°$ on the drive-shaft cover. The normal-force coefficient in figure 13(a) matches closely for all configurations from $\phi = -45°$ to $5°$ followed by a marked increase in c_z for the strake configurations through the critical range of ϕ. The side-force coefficients (fig. 13(b)) again are below those of the baseline configuration from $\phi = -20°$ to almost $10°$. An improved positive c_y can be found through the rest of the critical range of ϕ. These three configurations did not get the results desired throughout the critical range of ϕ.

With the upper strake located on the tail boom and the same three lower strake configurations (fig. 14(a)), there is an increase in c_z throughout the critical range compared with the baseline for all the strake configurations. Configuration S_7 has less of an increase in c_z throughout the critical range of ϕ than the other strake configurations. The side-force coefficient (fig. 14(b)) has a marked difference in appearance compared with those of the configurations with the strakes on the drive-shaft cover in that, compared with the baseline, there is no longer a reduced c_y in the range from $\phi = 0°$ to $40°$ for the three configurations. For configuration S_8, there is an increase in c_y from $\phi = -30°$ to $50°$ compared with the baseline. This configuration gave the best results for the OH-58A model through the critical range of ϕ due to the reduced side-force coefficient compared with the baseline. The reduction of the side-force co-

efficient was a product of the increased normal-force coefficient.

The data in figures 12 through 14 were used in calculations to determine a percentage of change that the strakes would have on a full-scale OH-58A at maximum gross weight (3000 lb). The equations used in the calculations were

$$S = b_1 D_1 \tag{1}$$

$$F_N = c_z \frac{1}{2} \rho v_s^2 S \tag{2}$$

$$\text{Change in main rotor horsepower} = \frac{\Delta F_N}{L_{P,mr}} \tag{3}$$

$$F_Y = c_y \frac{1}{2} \rho v_s^2 S \tag{4}$$

$$\text{Change in tail rotor horsepower} = \frac{\frac{D_2}{D_3} \Delta F_Y}{L_{P,tr}} \tag{5}$$

$$v = 1.69 v_s \tan \phi \tag{6}$$

The increased normal force (boom download) is compensated for by an increase in main rotor thrust. A positive side-force coefficient increment results in a decrease in tail rotor power required. The percents in power are based on the equations and the maximum rated power of a main rotor of 317 hp and a tail rotor power of 64 hp. These would represent the most conservative results. The sideward velocity in knots was computed by using the average slipstream velocity of the main rotor of an OH-58A and the tangent of ϕ (eq. (6)). The critical velocity range in terms of tail rotor power required was $v = 0$ to 30 knots in right sideward flight. This is the approximate range from hover to the point at which the main rotor downwash clears the tail boom.

Figure 15(a) shows that an average increase in main rotor power required during the critical range $v = 0$ to 30 knots was less then 1 percent. The peak increase in power required was 1.4 percent at 17 knots for configuration S_1. In figure 15(b) there was no reduction in tail rotor power required until $v = 10$ knots. The average reduction in tail rotor power for configurations S_1, S_2, and S_3 at $v = 0$ to 30 knots was less then 1 percent. The peak reduction in tail rotor power required in this range was about 4.0 percent for S_1, S_2, and S_3. In figure 16(a) for main rotor power required, the maximum increase was 1.4 percent for both S_4 and S_6 at $v = 17$ and 14 knots, respectively, and the average increase for the three configurations was less then 1 percent. The average tail rotor power reduction (fig. 16(b)) for configurations S_4 and S_5 from $v = 0$ to 30 knots is about 2.5 percent with a peak of 5.6 percent

at 17 knots for S_4. Configuration S_4 also had a maximum increase in tail rotor power required of 4.3 percent at 0 knot. The average decrease in tail rotor horsepower for configuration S_6 was only 1 percent. This was caused by the limited reduction in tail rotor power from 10 to 30 knots.

Figure 17 shows the results of the strake configurations with the upper strake placed on the tail boom at 60° from the vertical and the three different lower strake configurations. In figure 17(a), the average main rotor power requirement increase for configurations S_8 and S_9 is about 0.9 percent for $v = 0$ to 30 knots. The peak increase in main rotor power for S_9 was 1.3 percent at 14 knots. Configuration S_7 had a 0.6-percent average increase in main rotor power with a peak in main rotor power of 0.8 percent at 17 knots. The average tail rotor power requirements (fig. 17(b)) were reduced from $v = 0$ to 30 knots by less then 3 percent for configuration S_7 with a peak reduction in tail rotor power required of 4.4 percent at 14 knots. Configuration S_8 averaged 5.9 percent from $v = 0$ to 30 knots with a peak reduction in tail rotor power required of 7.7 percent at 5 knots. Configuration S_9 had a 4.7-percent average reduction in tail rotor power required with a peak of 8.5-percent reduction at 5 knots for configuration S_9. In summary, all strake configurations offered some decrease in tail rotor power for the OH-58A in the critical range $v = 0$ to 30 knots. Configuration S_8 was the most effective overall for the OH-58A over the widest range of airspeeds because it had a tail rotor power reduction average of 5.9 percent with no increase in tail rotor power throughout the critical airspeed range and less than 1 percent increase in main rotor power compared with the baseline. The overall power change was a 0.7-percent improvement for the OH-58A.

OH-58D Model Tail Boom Configurations

Testing methods and procedures used on the OH-58D tail boom model were similar to those on the OH-58A model discussed previously. The configurations consisted of the upper strake placed at 30° and 60° from the vertical on the drive-shaft cover or at 60° from the vertical on the tail boom of the OH-58D model. In addition, for each of the upper strake locations, the lower strake was placed at 150°, 180°, and 210° from the vertical on the tail boom. The results from these configurations were compared with the results from the OH-58D baseline configuration without strakes. As expected, since the only difference in the OH-58A and OH-58D models was the size of the drive-shaft cover, the data were similar.

In figure 18(a), c_z for configurations S_1, S_2, and S_3 was still approximately the same for $\phi = -40°$

to 10° with little or no difference compared with the baseline. For $\phi = 10°$ to 45°, these configurations had an increase in c_z. Configuration S_3 with the lower strake at 210° had a reduced c_z compared with the other strake configurations but only beyond $\phi = 30°$, the approximate range in which the main rotor downwash clears the tail boom. As with the OH-58A model, the poor results in c_y (fig. 18(b)) are still visible in configurations S_1, S_2, and S_3. From $\phi = -10°$ to almost 15°, there is a reduced side-force coefficient compared with that of the baseline, from $\phi = 15°$ to 40°, there is an improvement in c_y for these three configurations compared with the baseline. Because of the reduced side-force coefficient results compared with the baseline from $\phi = -10°$ to 15°, these three configurations would not improve the performance of the tail boom throughout the critical range $\phi = 0°$ to 45°.

Figure 19 shows a similar pattern with the strake at 60° on the drive-shaft cover compared with that of the strake at 30° on the drive-shaft cover except for a ϕ shift ($-10°$) for c_z (fig. 18(a)). For the three configurations at $\phi = -40°$ to 0°, c_z was relatively the same as for the baseline or slightly reduced. Starting at $\phi = 0°$, c_z for the three straked configurations increased above the baseline through $\phi = 45°$. Configuration S_6 reduced c_z from $\phi = 30°$ through 90° compared with S_4 and S_5. The side-force coefficient results in figure 19(b) were also similar to those for configurations S_1, S_2, and S_3 (fig. 18(b)) with the upper strake at 30° on the drive-shaft cover. From $\phi = -20°$ to 5°, there is a reduced side-force coefficient compared with that for the baseline from the strake application for all three configurations (S_4, S_5, and S_6). From $\phi = 5°$ through 10°, there is an improvement over the baseline. This trend continues until $\phi = 60°$ for configuration S_5 and $\phi = 90°$ for S_4. Configurations S_4, S_5, and S_6 do not offer significant improvement of the side-force coefficient throughout the critical range $\phi = 0°$ to 45°.

Similar to the OH-58A, when the upper strake was placed on the tail boom at 60° for configurations S_7, S_8, and S_9, the results changed compared with the baseline for both c_z and c_y. In figure 20(a) there is an increase in c_z throughout the critical range until $\phi = 40°$ for all three strake configurations compared with the baseline. The lower strake changes in angular location have relatively no influence on this increase during the critical range $\phi = 0°$ to 45°. The c_y results for these configurations (S_7, S_8, and S_9) in figure 20(b) are quite different than the previous six configurations (S_1 through S_6) with the upper strake located on the drive-shaft cover. From $\phi = -25°$ to 40° for configuration S_7, there is an improvement over the baseline for the side-force coefficient. For

configuration S_8 there is the same improvement from $\phi = -25°$ to $50°$, and for configuration S_9 the improvement was from $\phi = -25°$ to $35°$. These three configurations (S_7, S_8, and S_9) offered the best results in a positive change in c_y throughout the critical range of $\phi = 0°$ to $45°$. Configuration S_8 gave the best results in c_y for the OH-58D model.

The data from figures 18 though 20 were used as input to equations (1) through (6) to calculate the percent changes that the strakes have on a full-scale OH-58D helicopter at maximum gross weight (4500 lb). The calculations used the two-dimensional data taken at a tunnel dynamic pressure of 15 psf. As with the OH-58A data, the normal force (download on the tail boom) is compensated for by an increase in main rotor power, and an increased side-force coefficient is shown as a decrease in tail rotor power. A main rotor power of 586 hp and a tail rotor power of 110 hp were used as the basis to derive these percents. Again the sideward velocity was computed by using an average slipstream velocity of the main rotor of the OH-58D and the tangent of the angle ϕ (eq. (6)), and the critical velocity range is $v = 0$ to 30 knots. In figure 21(a), the main rotor power had less than 1 percent average increase for configurations S_1, S_2, and S_3 from $v = 0$ to 30 knots. The peak increase in power was 1.3 percent at 21 knots for configuration S_2. The tail rotor power (fig. 21(b)) does not show a reduction until $v = 10$ knots for all three configurations. The maximum increase in tail rotor required was 4.0 percent at 5 knots for configuration S_1. This affected the overall improvement within the critical range $v = 0$ to 30 knots. All three configurations had 1.3 percent or less average reduction for this range with a peak of 4.2 percent at 17 knots for configurations S_1 and S_2.

In figure 22(a) the main rotor power increase for configurations S_4, S_5, and S_6 averaged about 1 percent for the range of $v = 0$ to 30 knots with peaks of about 1.4 percent at 17 to 21 knots. The tail rotor power average benefit (fig. 22(b)) for these configurations was hampered by the increase in the percentage of tail rotor power required from $v = 0$ to 6 knots. All configurations had a maximum increase in tail rotor power required of 5 percent at 0 knot. The average results from the critical range for configuration S_4 was 2.3 percent and for configuration S_5 was 2.1 percent. The configuration with the best results for tail rotor power was configuration S_6 with an average reduction of 2.7 percent in tail rotor power required and a peak reduction at 21 knots of 5.4 percent.

Figure 23 shows the effect of locating the upper strake on the tail boom at 60° with three lower strake

locations. The effect on main rotor power during the critical range shown in figure 23(a) for each of the three configurations averages less than 0.6 percent. The peak increase in main rotor power required was 1.1 percent at 13 knots for configuration S_9. The tail rotor power reduction for these configurations shown in figure 23(b) improved significantly as expected from the data in figure 20(b). Configuration S_7 had a 3.6-percent average improvement in tail rotor power throughout the critical airspeed range. Although configuration S_9 had a peak reduction in tail rotor power of 6.7 percent at 10 knots, it had an adverse effect above $v = 20$ knots, which brought the average throughout the critical range of v down to 3 percent. Configuration S_8 had a reduction of 4.4 percent of the tail rotor power required with a peak of 6.2 percent at 3 knots. Configuration S_8 also had less than a 0.6-percent increase in main rotor power to give this configuration an overall net improvement of 0.5 percent, therefore, configuration S_8 was the most effective at reducing the tail rotor power required for this investigation on the OH-58D tail boom.

Summary of Results

An investigation was made in the Langley 14- by 22-Foot Subsonic Tunnel on two-dimensional models of a circular cylinder and on tail boom cross sections representative of OH-58A and OH-58D helicopters. The purpose was to determine two-dimensional aerodynamic force coefficients on these models and the effect of adding strakes to the models over a flow incidence ϕ range from $-45°$ to $90°$. This range represents sideward flight. The data were used to calculate the percent change in main rotor and tail rotor horsepower for each configuration. The results are summarized as follows:

1. The placement of a 2-inch-high strake at 60° from the vertical and a 1-inch-high strake at 180° from the vertical on the OH-58A or the OH-58D models gave the best results for improving the side-force coefficient compared with the baseline models during the critical range of ϕ. As expected, these configurations also showed an increase in download on the tail boom.

2. Calculations derived from data from the best configuration indicated that the tail rotor power required was reduced by an average of about 6 percent in the critical right sideward velocity range of 0 to 30 knots for the OH-58A and an average of about 4.4 percent for the OH-58D under the same conditions.

3. The download penalty caused by the strake configurations which gave the best results (60° and 180° on the tail boom) through the critical sideward velocity range was calculated to be about

0.5 percent of main rotor power for OH-58A and OH-58D helicopters.

4. Placement of strakes on the drive-shaft cover of the OH-58A and OH-58D models reduced the side-force coefficient compared with that of the baseline only from $\phi = -10°$ to 15°; therefore, these configurations were not effective through the critical range of ϕ.

5. The bottom placement of a strake on the tail boom models showed the best overall results at 180° when compared with the 210° and 150° placements. At 210° the strake was effective at reducing the normal-force (download) coefficient but also reduced the side force (side-load) coefficient effectiveness compared with that of the baseline during the critical range of ϕ. The results of the strake at 150° were similar to those of the 180° placement but were not quite as effective in increasing side-force coefficient.

References

1. Blake, Bruce; Hodder, David St. J.; and Hanker, Edward J., Jr.: *Wind Tunnel Investigation Into the Directional Control Characteristics of an OH-58A Helicopter.* USAAVRADCOM TR-83-D-18, U.S. Army, June 1984. (Available from DTIC as AD B084 796L.)

2. McKee, John W.: *Experimental Investigation of the Pressure Fluctuations on a Flat Plate and a Cylinder in the Slipstream of a Hovering Rotor.* NASA TN D-112, 1959.

3. Polhamus, Edward C.: *Effect of Flow Incidence and Reynolds Number on Low-Speed Aerodynamic Characteristics of Several Noncircular Cylinders With Applications to Directional Stability and Spinning.* NASA TR R-29, 1959. (Supersedes NACA TN 4176.)

4. Polhamus, Edward C.; Geller, Edward W., and Grunwald, Kalman J.: *Pressure and Force Characteristics of Noncircular Cylinders as Affected by Reynolds Number With*

a Method Included for Determining the Potential Flow About Arbitrary Shapes. NASA TR R-46, 1959.

5. Lockwood, Vernard E.; and McKinney, Linwood W.: *Effect of Reynolds Number on the Force and Pressure Distribution Characteristics of a Two-Dimensional Lifting Circular Cylinder.* NASA TN D-455, 1960.

6. Taylor, P.: A Method of Predicting Fuselage Loads in Hover. Seventh European Rotorcraft and Powered Lift Aircraft Forum, Deutsche Gesellschaft fur Luft- und Raumfahrt e. v., Sept. 1981, Paper No. 49.

7. Achenbach, E.; and Heinecke, E.: On Vortex Shedding From Smooth and Rough Cylinders in the Range of Reynolds Numbers 6×10^3 to 5×10^6. *J. Fluid Mech.,* vol. 109, Aug. 1981, pp. 239–251.

8. Fage, A., and Warsap, J. H.: *The Effects of Turbulence and Surface Roughness on the Drag of a Circular Cylinder.* R. & M. No. 1283, British Aeronautical Research Council, 1930.

9. Wilson, John C.; and Kelley, Henry L.: *Aerodynamic Characteristics of Several Current Helicopter Tail Boom Cross Sections Including the Effect of Spoilers.* NASA TP-2506, AVSCOM TR 85-B-3, 1986.

10. Lockwood, Roy A.; Kelly, William A.; and Cason, Randall W.: *Flight Characteristics Test of the UH-60A With Tail Boom Mounted Strake.* USAAEFA Proj. No. 85-07, U.S. Army, Oct. 1986.

11. Wilson, John C.; Kelley, Henry L.; Donahue, Cynthia C.; and Yenni, Kenneth R.: *Developments in Helicopter Tail Boom Strake Applications in the United States.* NASA TM-101496, AVSCOM TM-88-B-014, 1988.

12. Kelley, Henry L., Crowell, Cynthia A., Yenni, Kenneth R., and Lance, Michael B.: Flight Investigation of the Effect of Tail Boom Strakes on Helicopter Directional Control. *46th Annual Forum and Technology Display,* American Helicopter Soc., 1990, pp. 1161–1174.

13. Rae, William H., Jr.; and Pope, Alan. *Low-Speed Wind Tunnel Testing,* Second ed. John Wiley & Sons, Inc., c.1984.

14. Schlichting, Hermann (J. Kestin, transl.). *Boundary-Layer Theory,* Seventh ed. McGraw-Hill Book Co., c.1979.

15. Gentry, Garl L., Jr.; Quinto, P. Frank; Gatlin, Gregory M., and Applin, Zachary T.: *The Langley 14- by 22-Foot Subsonic Tunnel. Description, Flow Characteristics, and Guide for Users.* NASA TP-3008, 1990.

Table I. Strake Configurations

Configuration	Height, in.	Angular position
OH-58A and OH-58D models		
S_1	2	30° from top of drive-shaft cover centerline
	1	150° from top of tail boom centerline
S_2	2	30° from top of drive-shaft cover centerline
	1	180° from top of tail boom centerline
S_3	2	30° from top of drive-shaft cover centerline
	1	210° from top of tail boom centerline
S_4	2	60° from top of drive-shaft cover centerline
	1	150° from top of tail boom centerline
S_5	2	60° from top of drive-shaft cover centerline
	1	180° from top of tail boom centerline
S_6	2	60° from top of drive-shaft cover centerline
	1	210° from top of tail boom centerline
S_7	2	60° from top of tail boom centerline
	1	150° from top of tail boom centerline
S_8	2	60° from top of tail boom centerline
	1	180° from top of tail boom centerline
S_9	2	60° from top of tail boom centerline
	1	210° from top of tail boom centerline
Cylinder model		
S_a	2	30° from top of tail boom centerline
	1	150° from top of tail boom centerline
S_b	2	60° from top of tail boom centerline
	1	150° from top of tail boom centerline
S_c	2	60° from top of tail boom centerline
	1	180° from top of tail boom centerline
S_d	2	60° from top of tail boom centerline
	1	210° from top of tail boom centerline
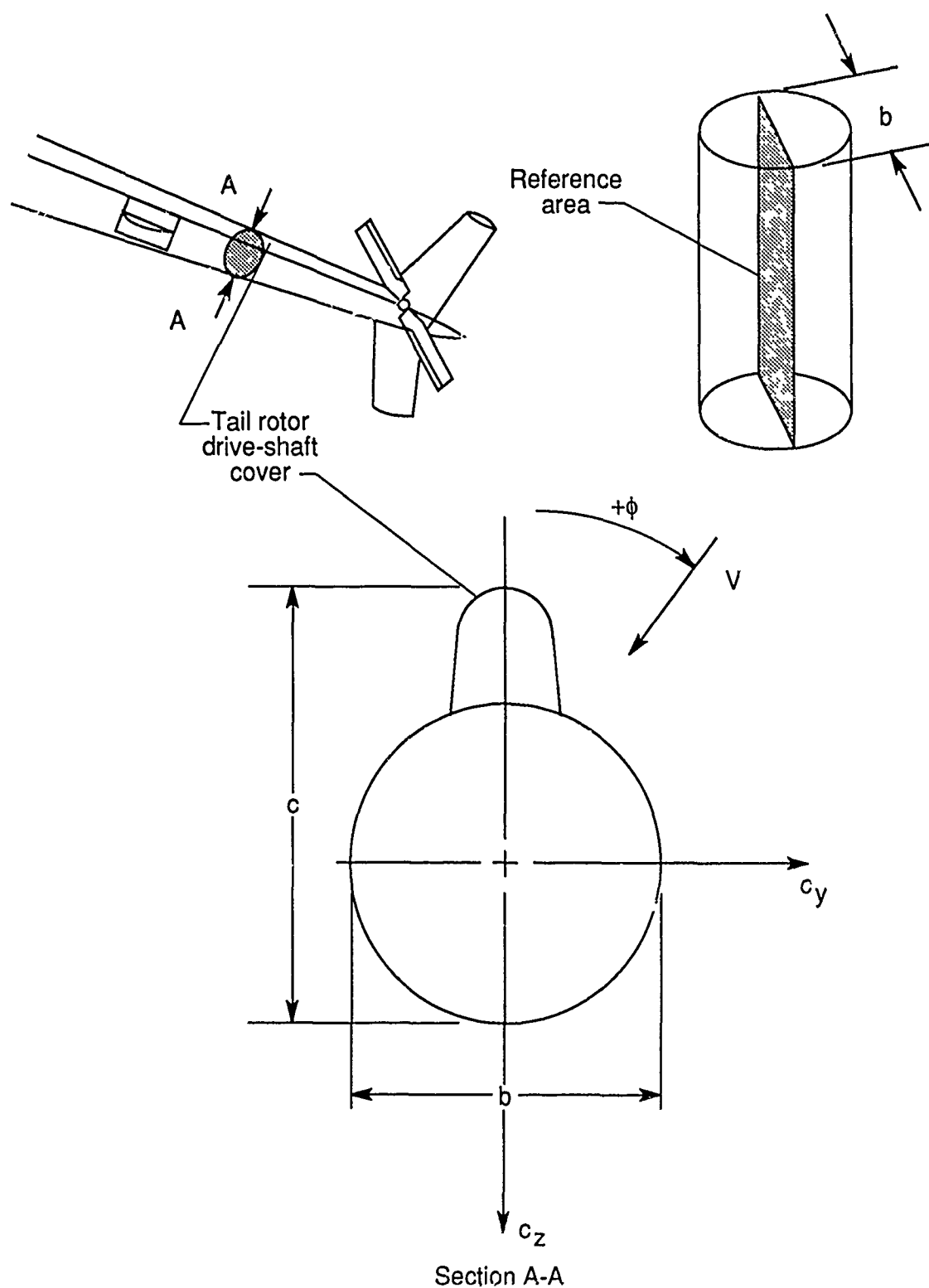
Figure 1. Convention for positive sense of flow inclination, cylinder reference dimensions, and aerodynamic coefficients.
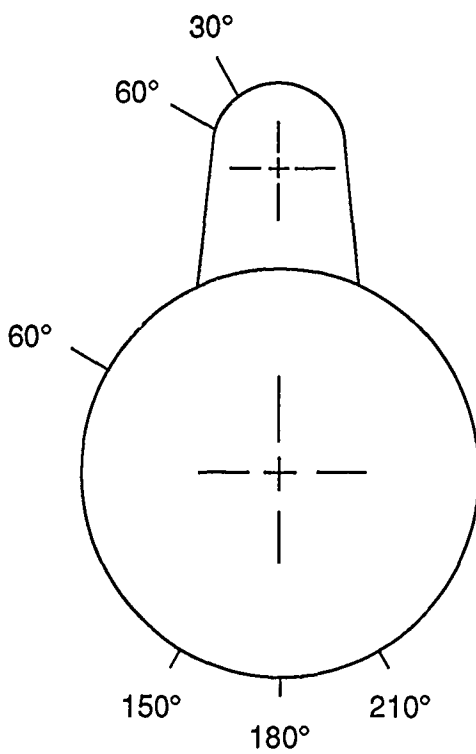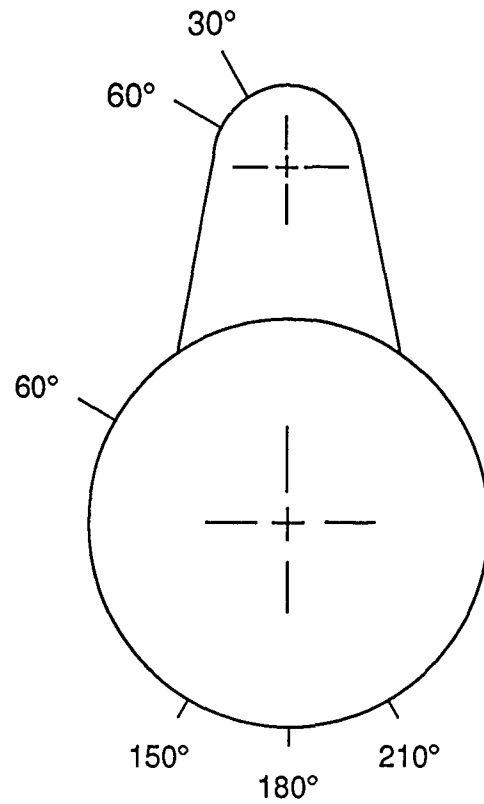
Figure 2. Strake placement on model cross sections of cylinder, OH-58A, and OH-58D tail boom shapes. Upper strakes measured 2 in. high and lower strakes measured 1 in.
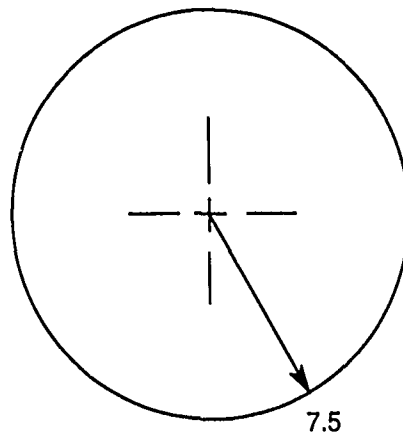
(a) Cylinder.
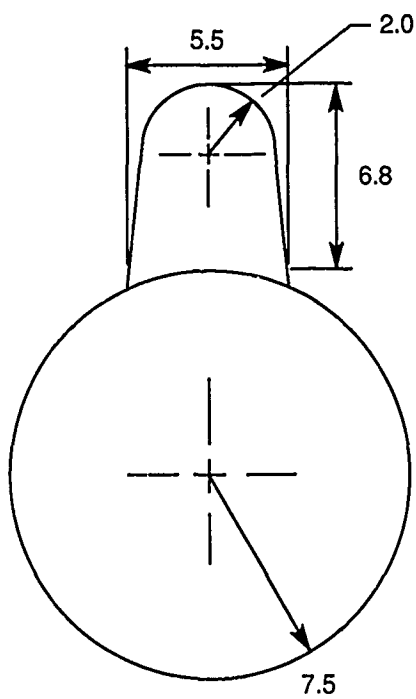
(b) OH-58A.
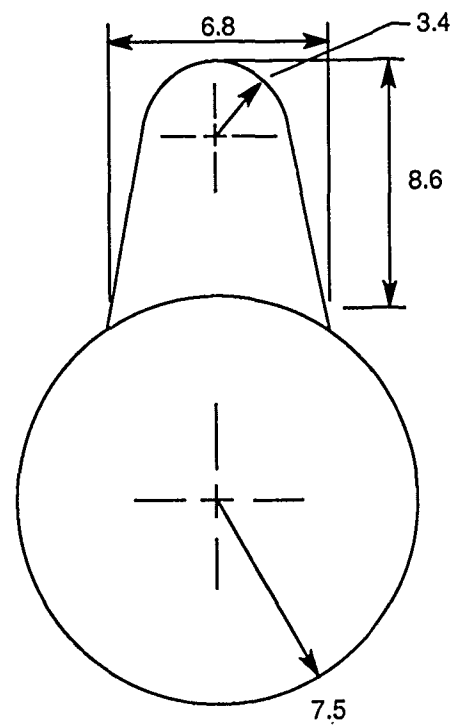
(c) OH-58D.

Figure 3. Model cross sections of cylinder, OH-58A, and OH-58D tail boom shapes. Dimensions are in inches.
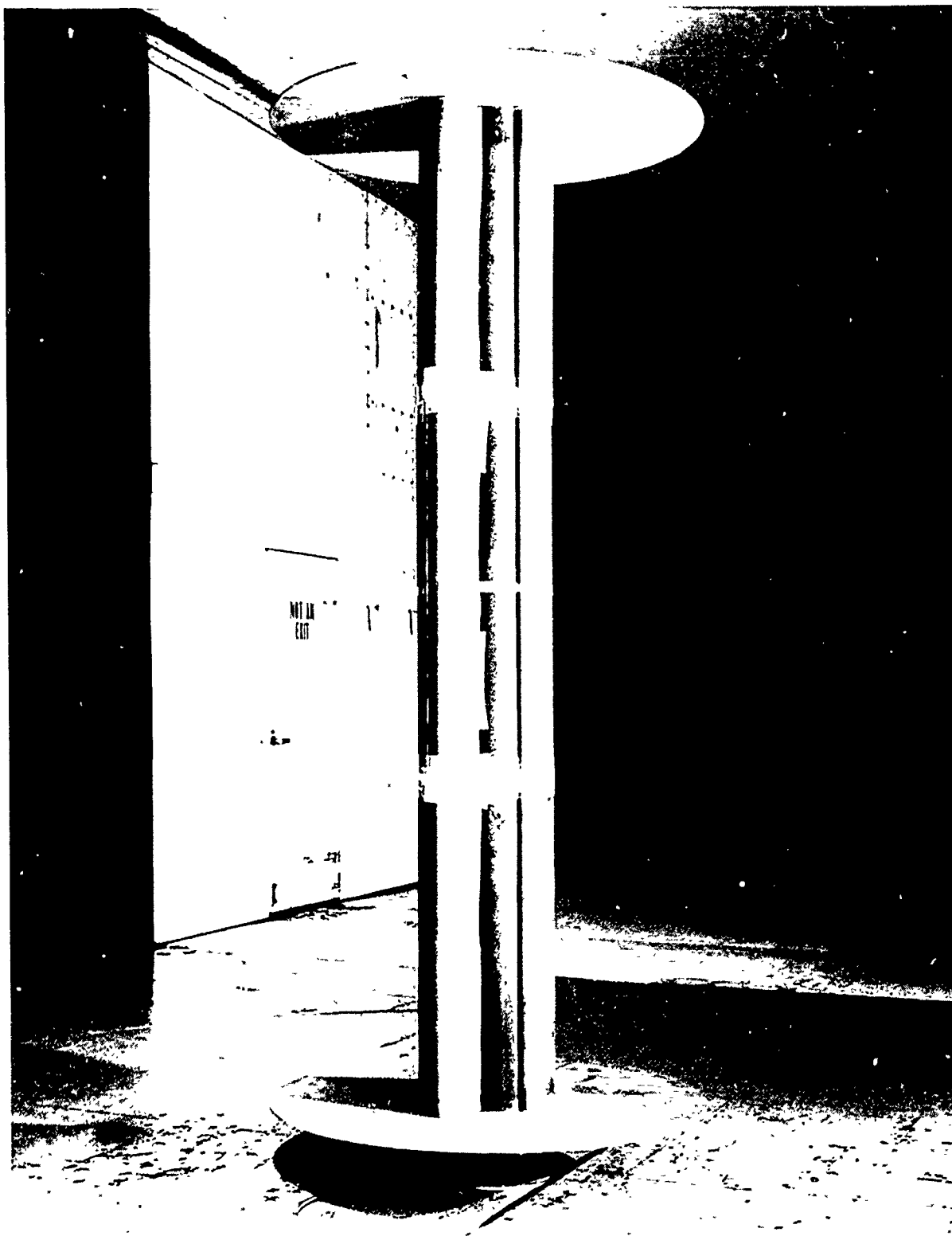
L-82-6842

Figure 4. Two-dimensional test apparatus in Langley 14- by 22-Foot Subsonic Tunnel.
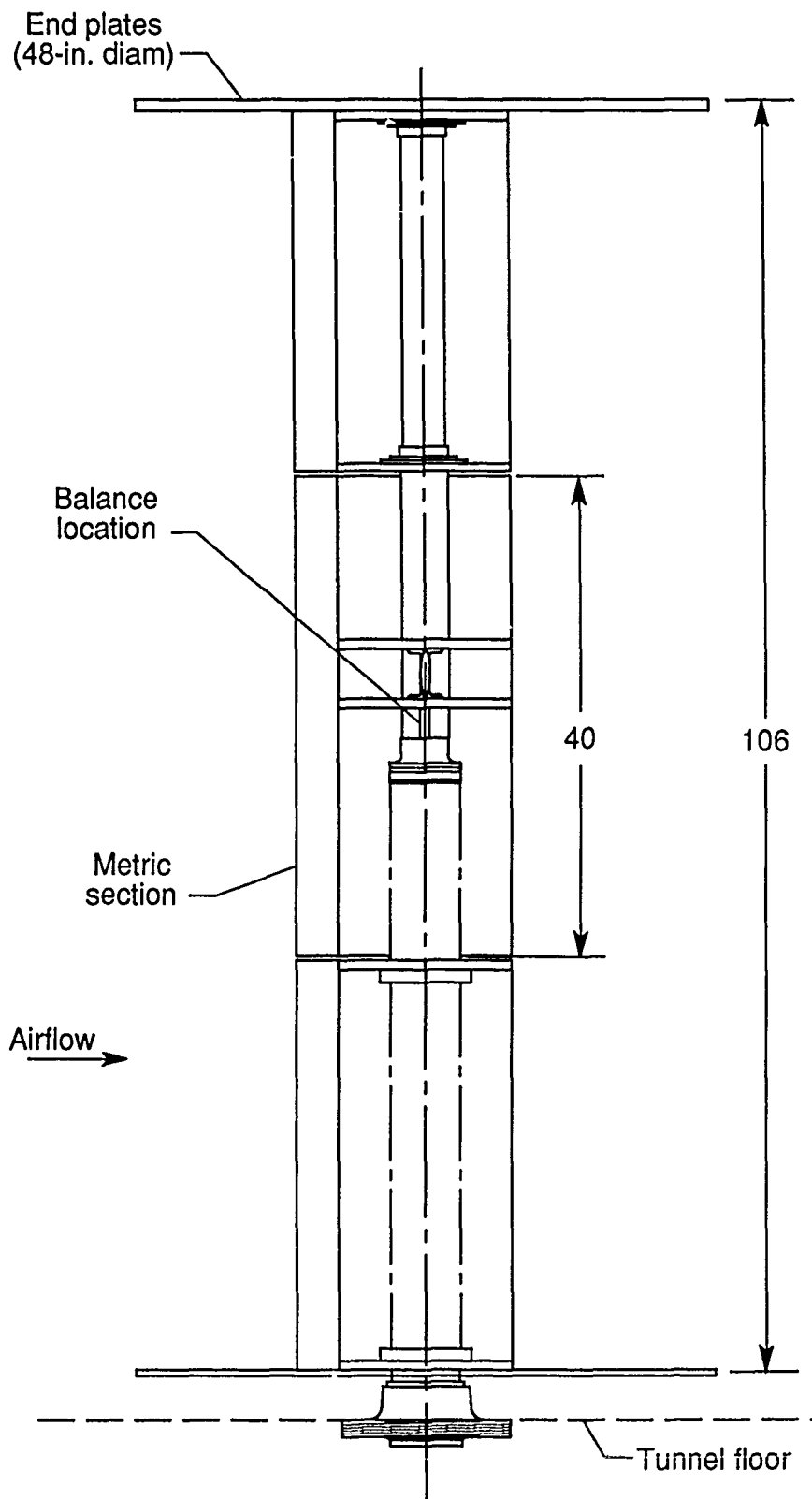
Figure 5. Schematic drawing of helicopter cross-sectional test apparatus. Dimensions are in inches.
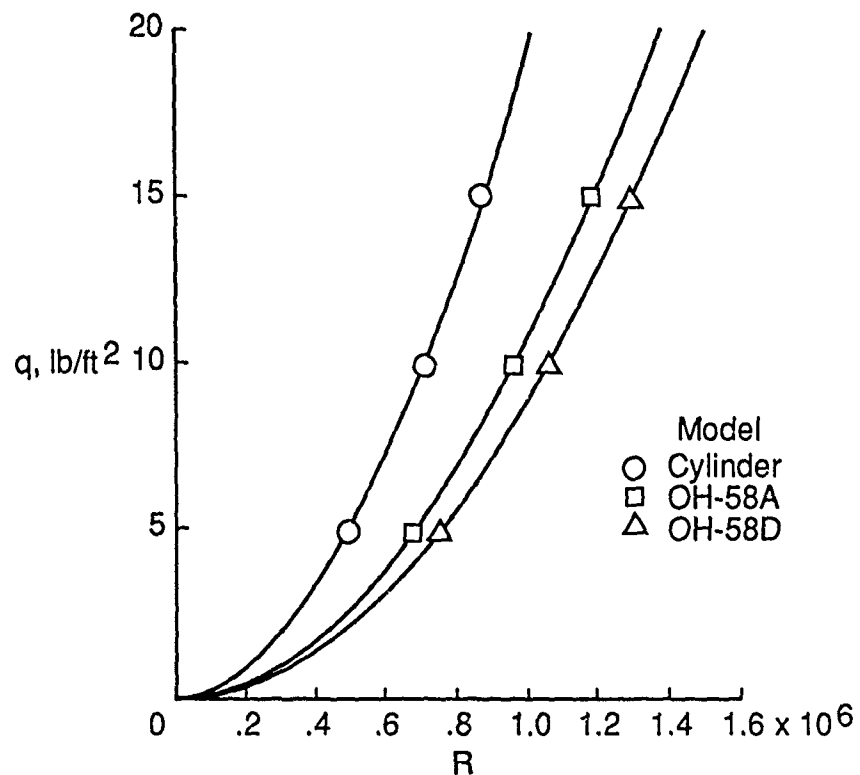
Figure 6. Test dynamic pressure as function of Reynolds number.
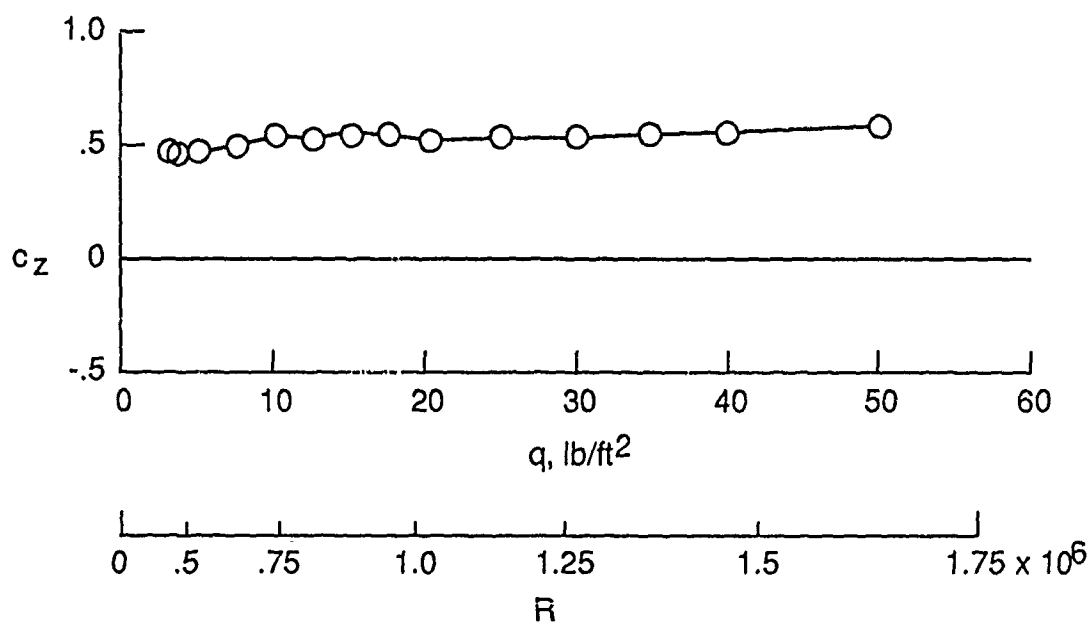
Figure 7. Effect of q and R on c_z of cylinder model.
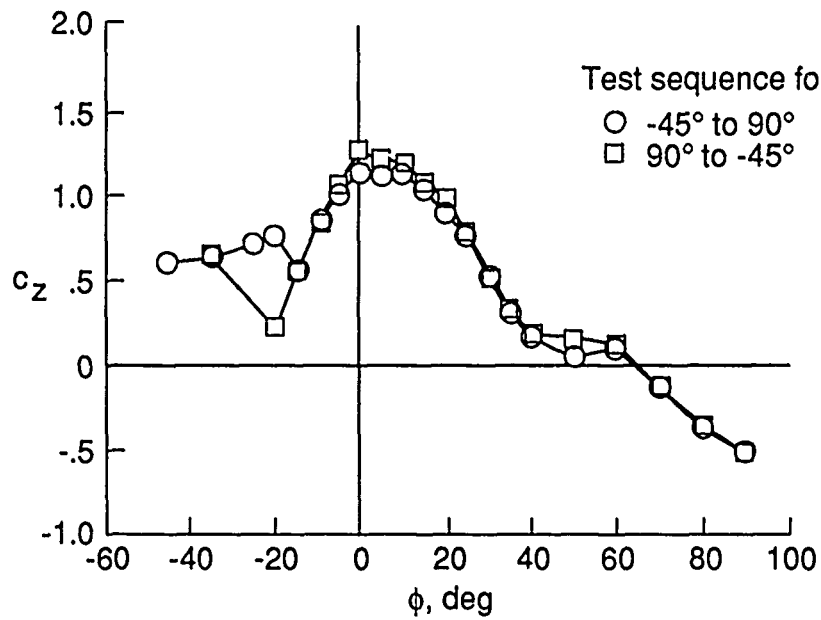
(a) Normal-force coefficient.
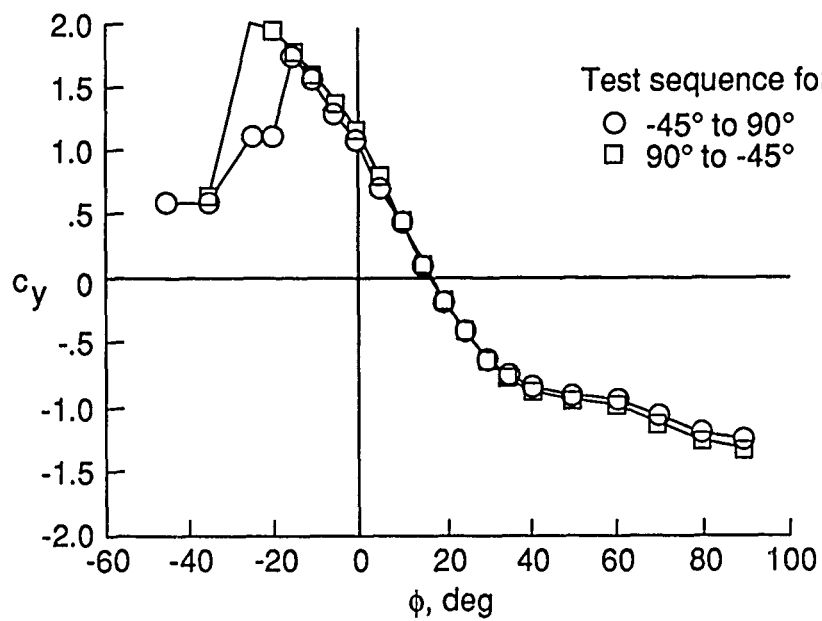
(b) Side-force coefficient.

Figure 8. Effect of changing ϕ to determine hysteresis effects. Configuration S_8 (OH-58D model).
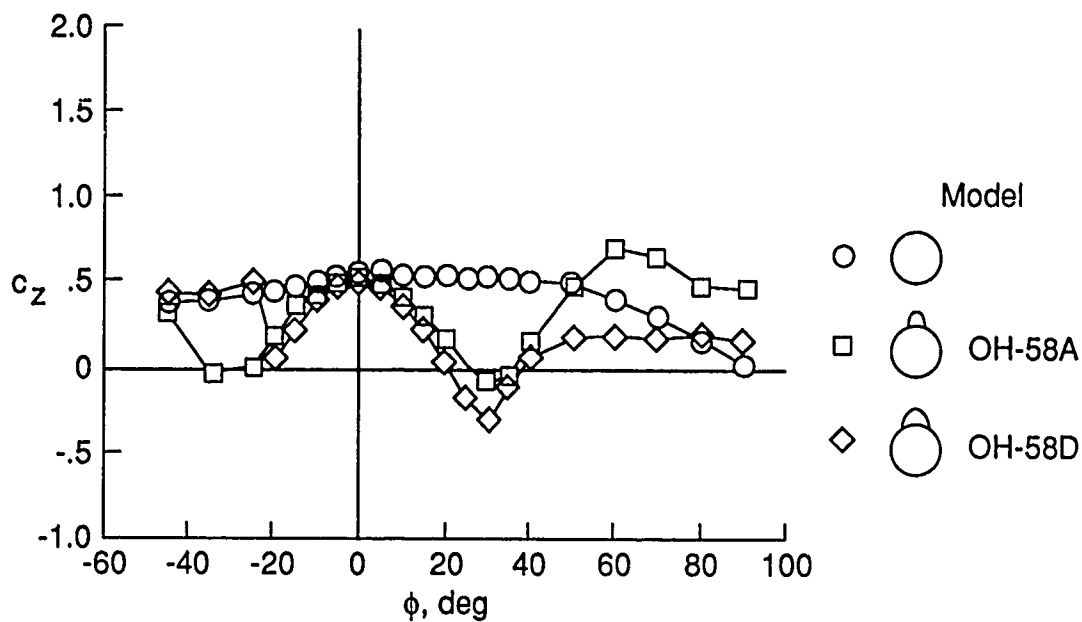
(a) Normal-force coefficient.
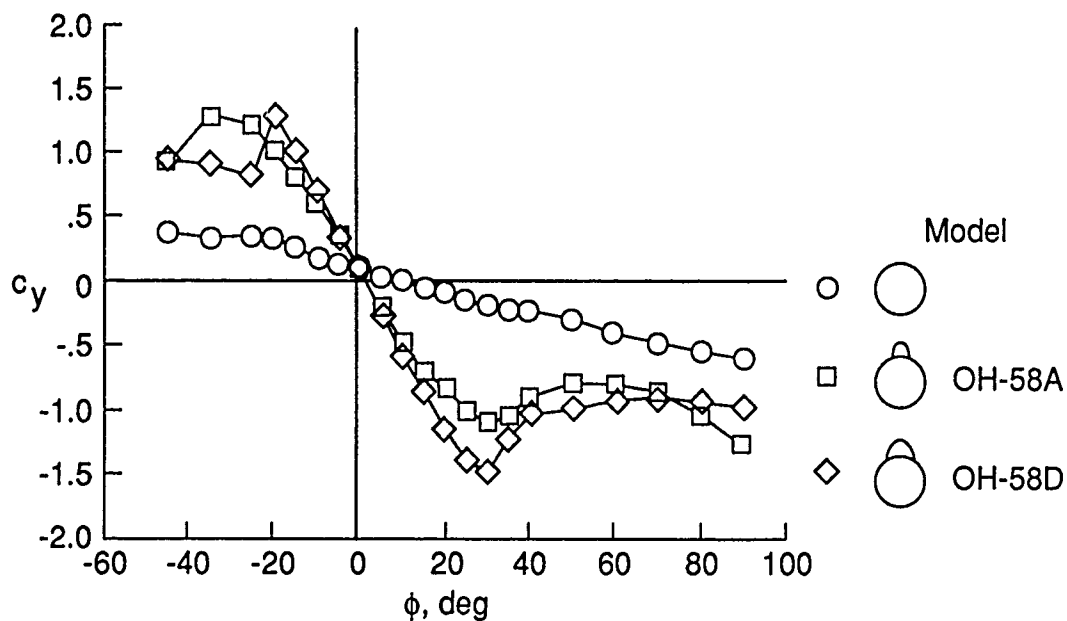
(b) Side-force coefficient.

Figure 9. Effect of flow incidence on c_z and c_y for cylinder, OH-58A, and OH-58D tail boom models.

17
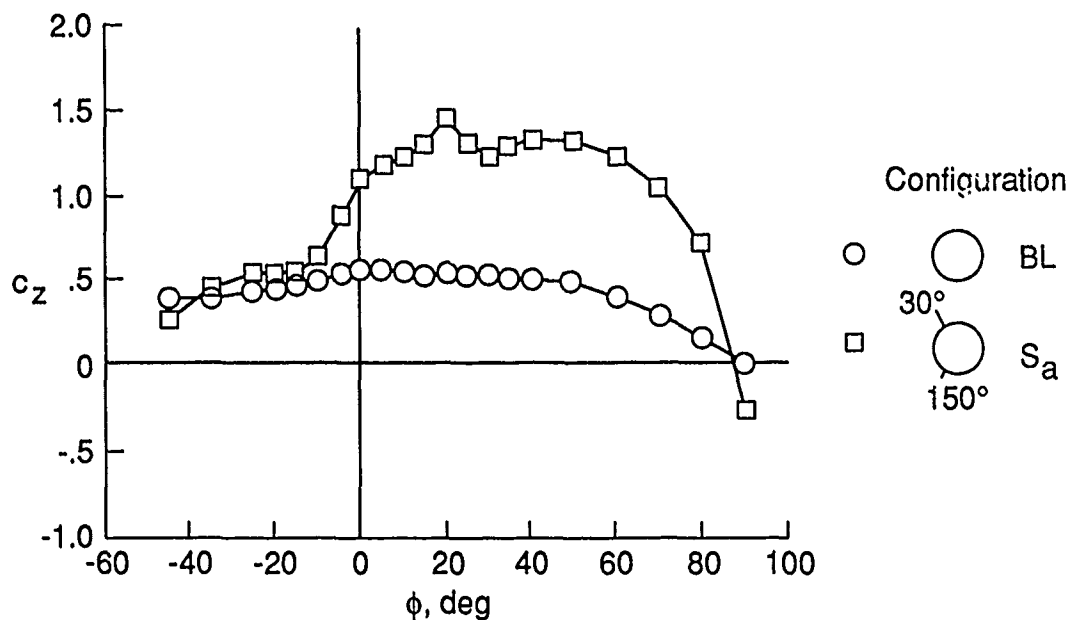
(a) Normal-force coefficient.
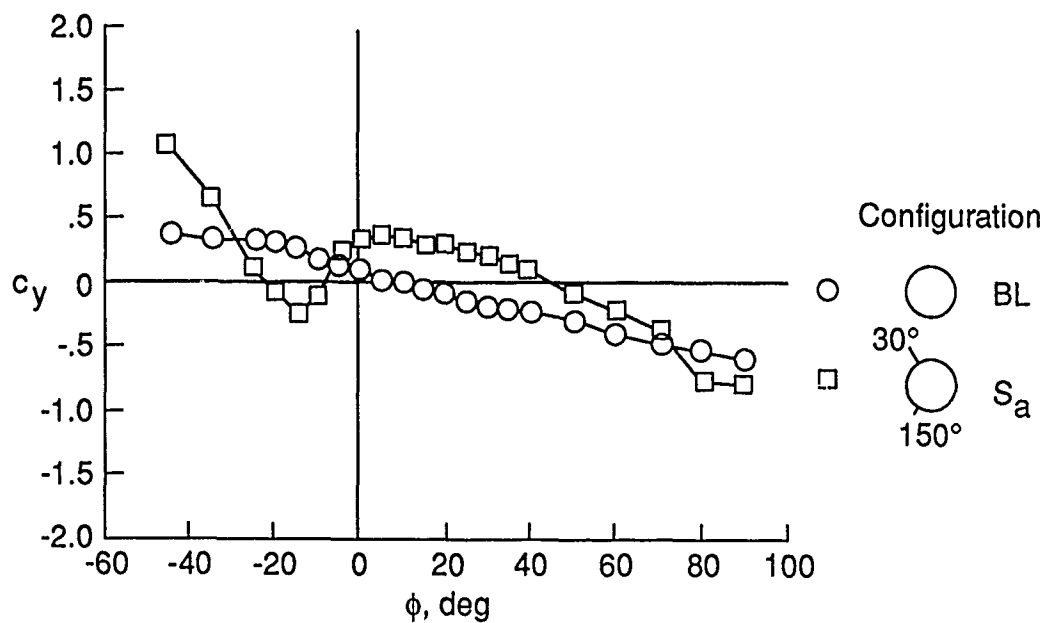
(b) Side-force coefficient.

Figure 10. Effect of flow incidence on c_z and c_y for cylinder and configuration S_a.
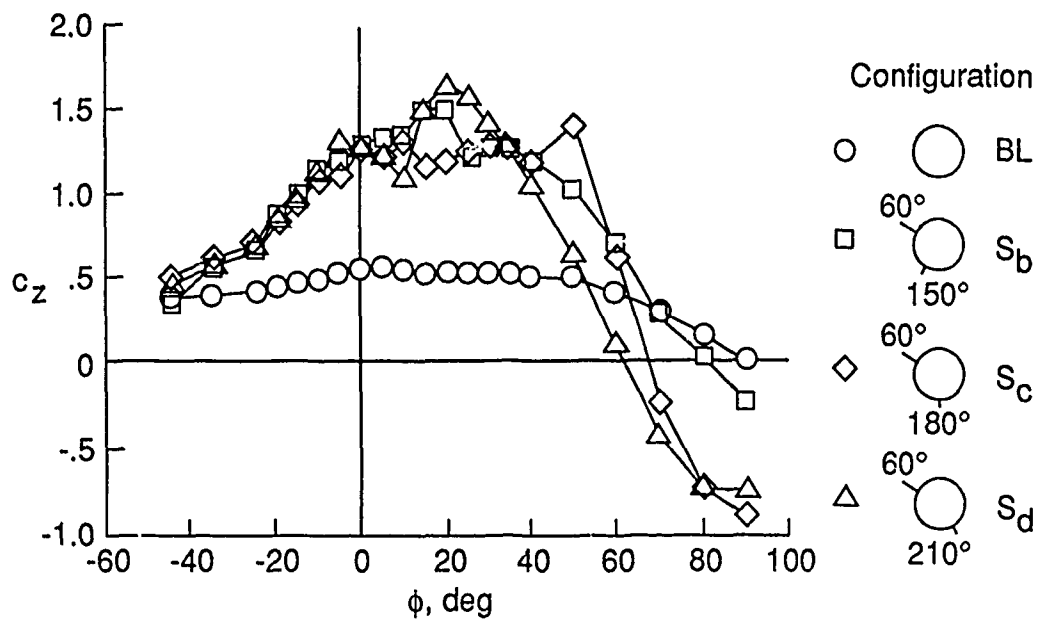
(a) Normal-force coefficient.
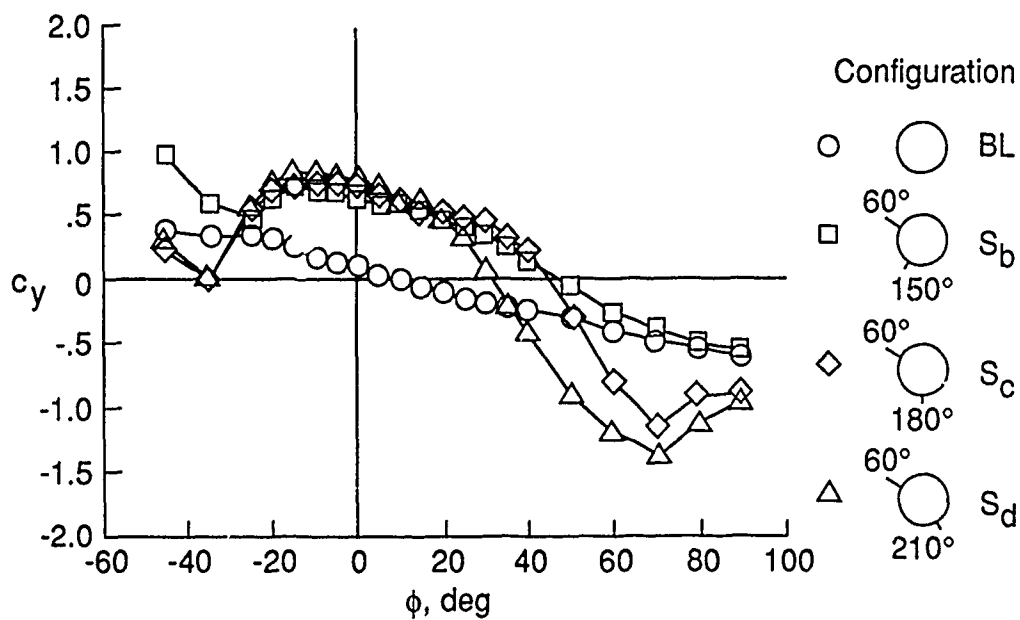
(b) Side-force coefficient.

Figure 11. Effect of flow incidence on c_z and c_y for cylinder and configurations S_b, S_c, and S_d.
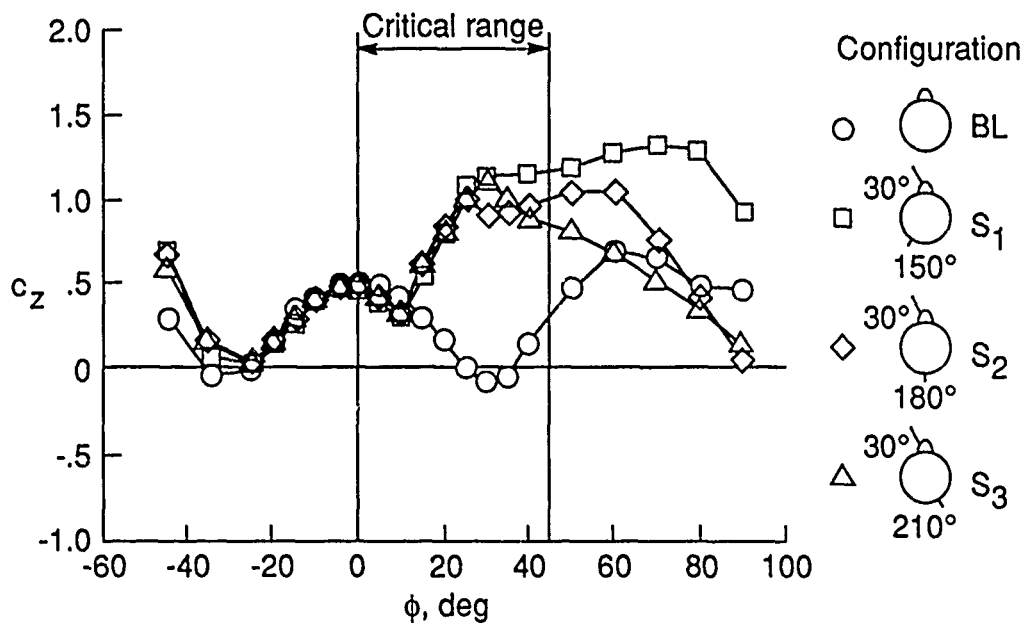
(a) Normal-force coefficient.
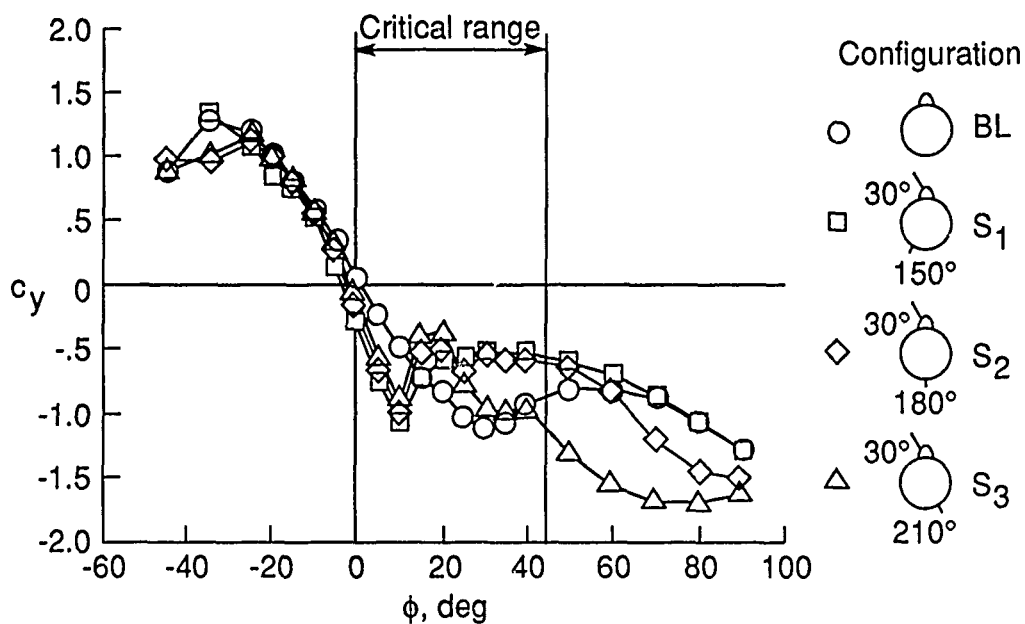
(b) Side-force coefficient.

Figure 12. Effect of flow incidence on c_z and c_y for OH-58A shape and configurations S_1, S_2, and S_3.
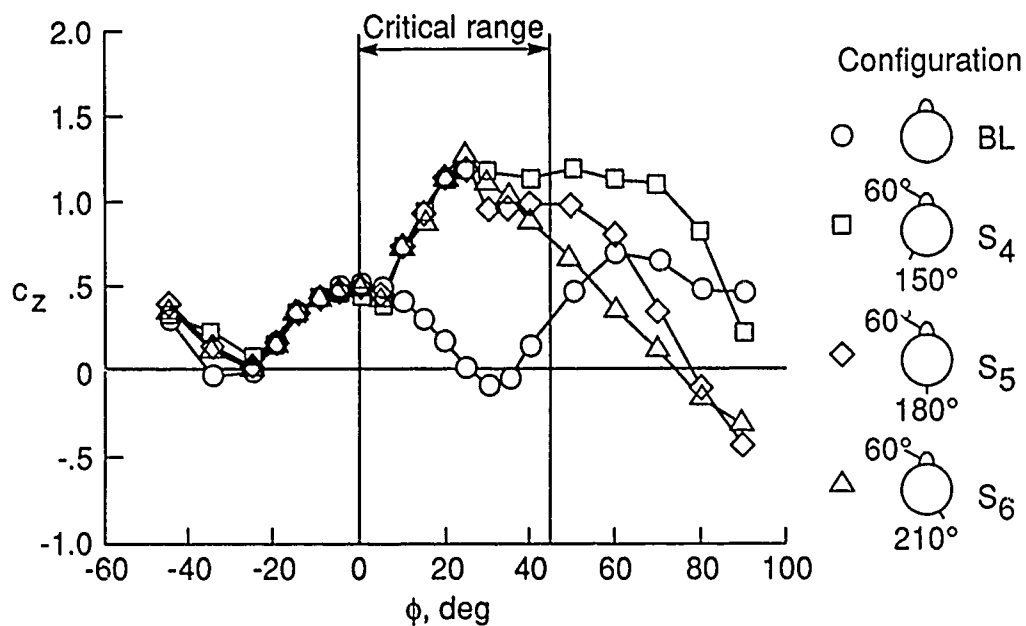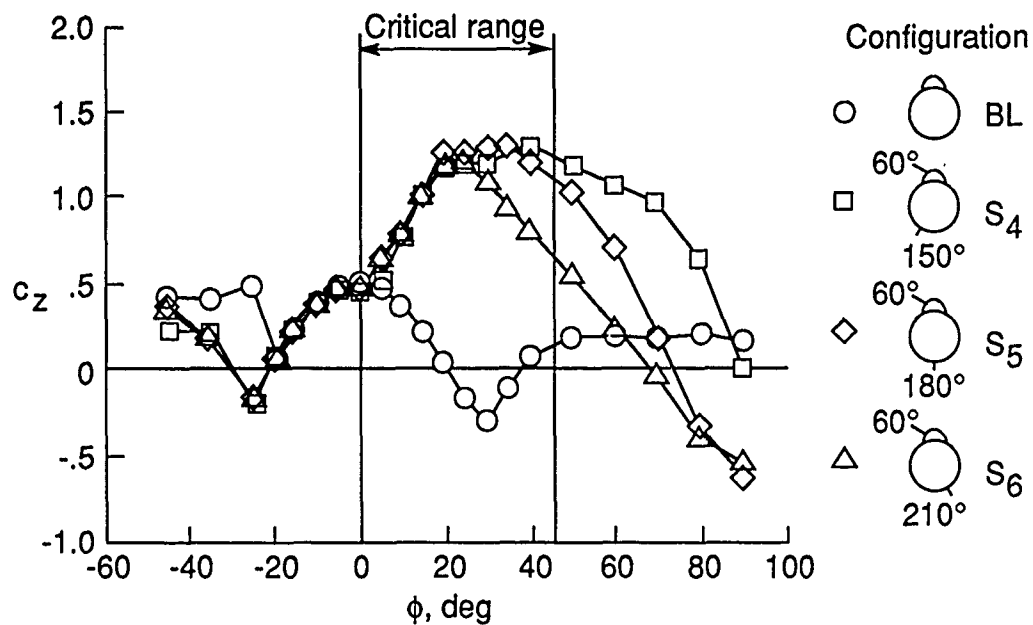
(a) Normal-force coefficient.
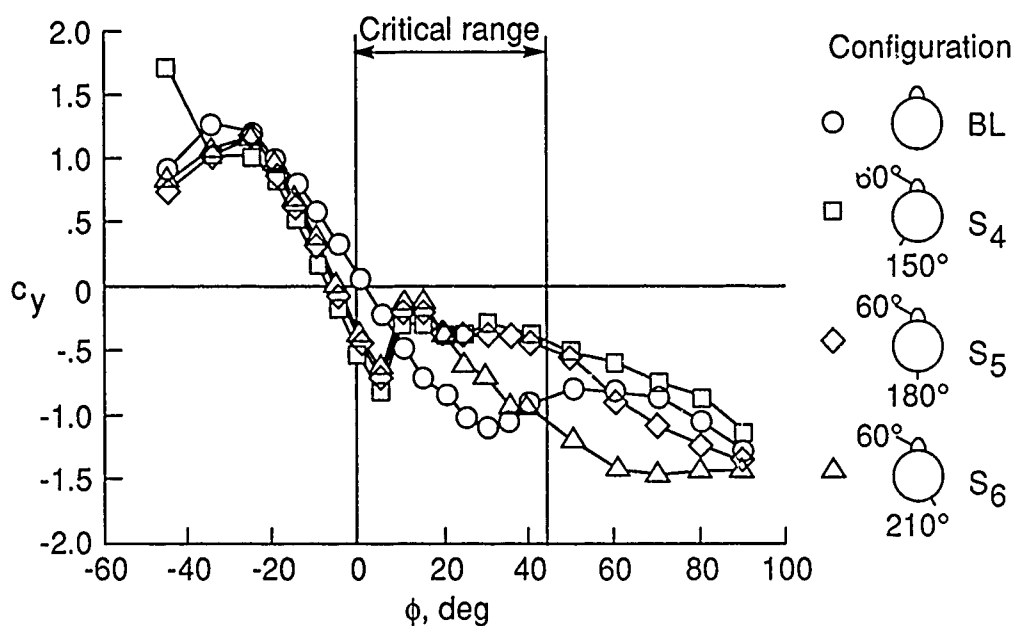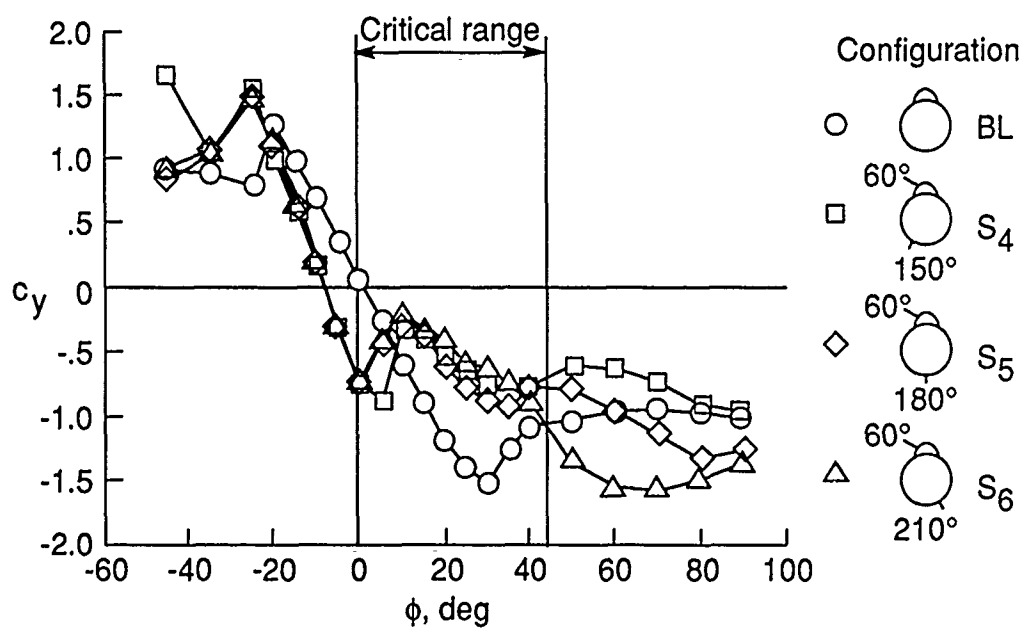

(b) Side-force coefficient.

Figure 13. Effect of flow incidence on c_z and c_y for OH-58A shape and configurations S_4, S_5, and S_6.
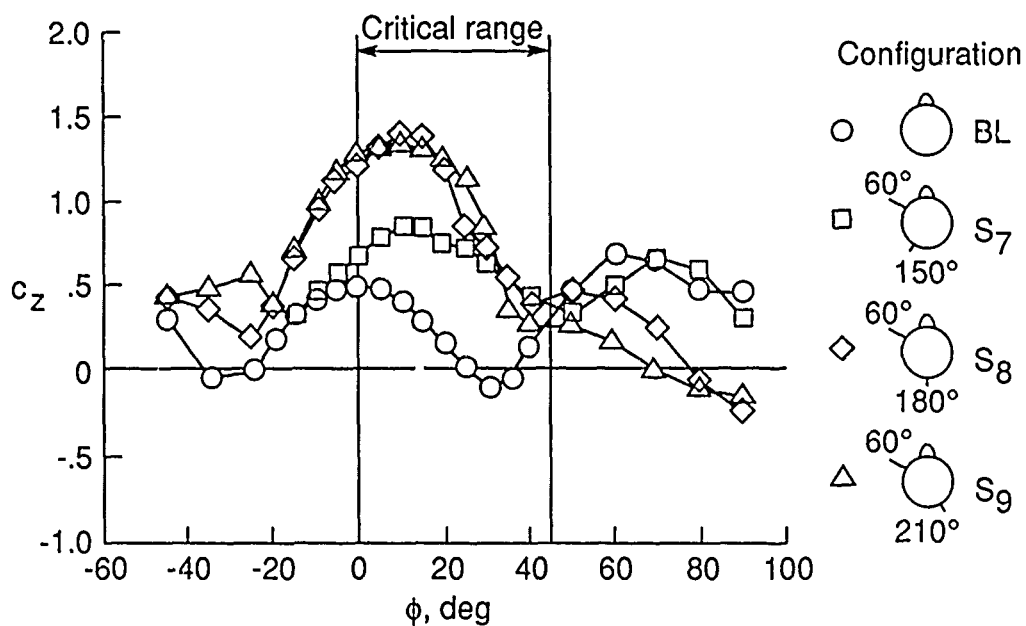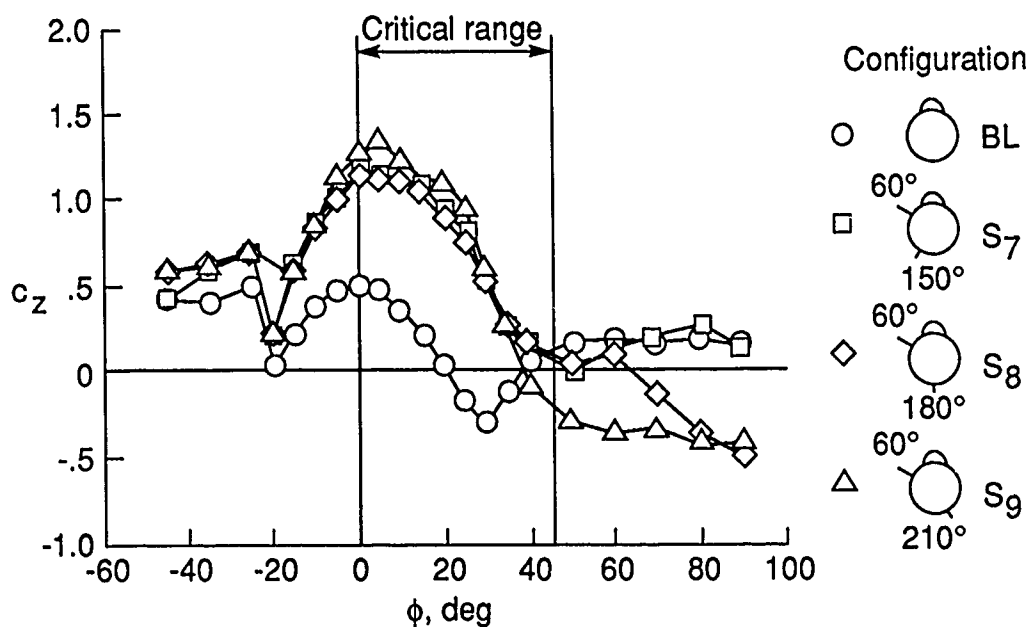
(a) Normal-force coefficient.
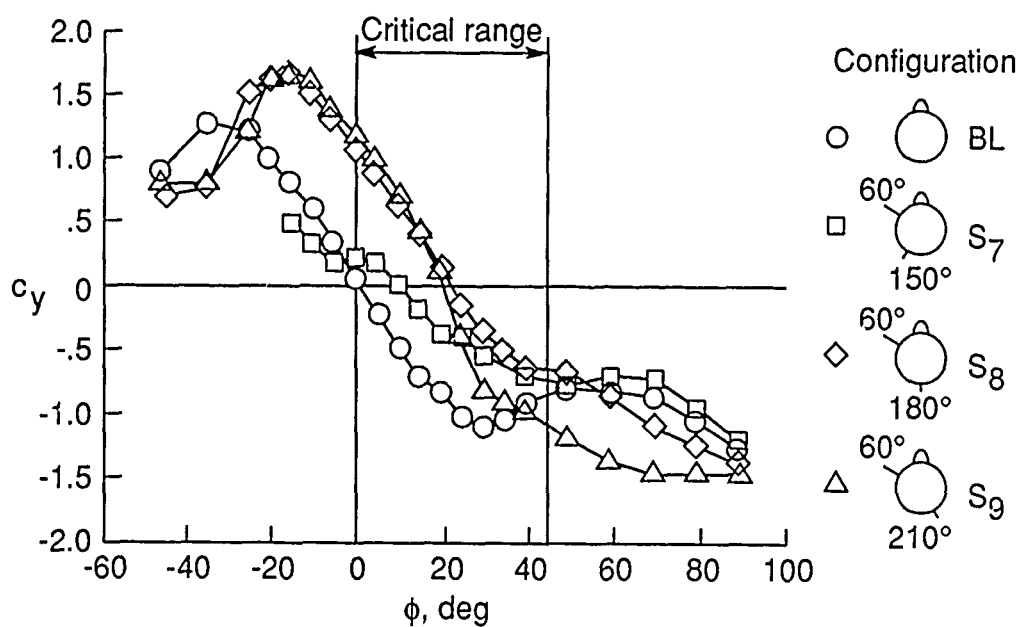
(b) Side-force coefficient.

Figure 14. Effect of flow incidence on c_z and c_y for OH-58A shape and configurations S_7, S_8, and S_8.
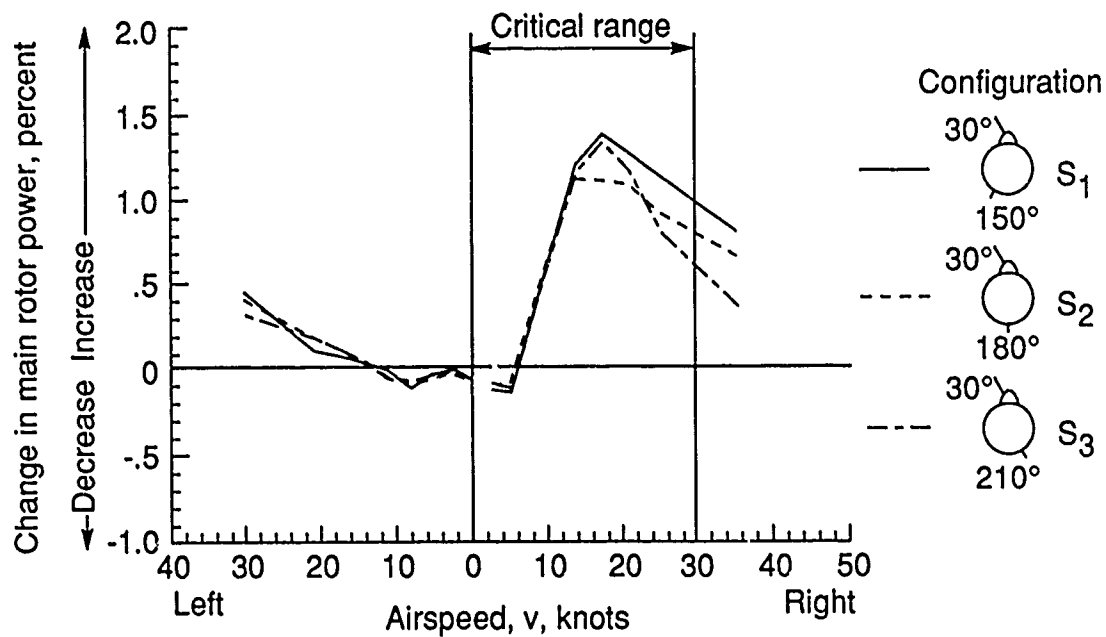
(a) Main rotor power.

(b) Tail rotor power.

Figure 15. Calculated change in rotor power as function of airspeed for configurations S_1, S_2, and S_3 of OH-58A model.
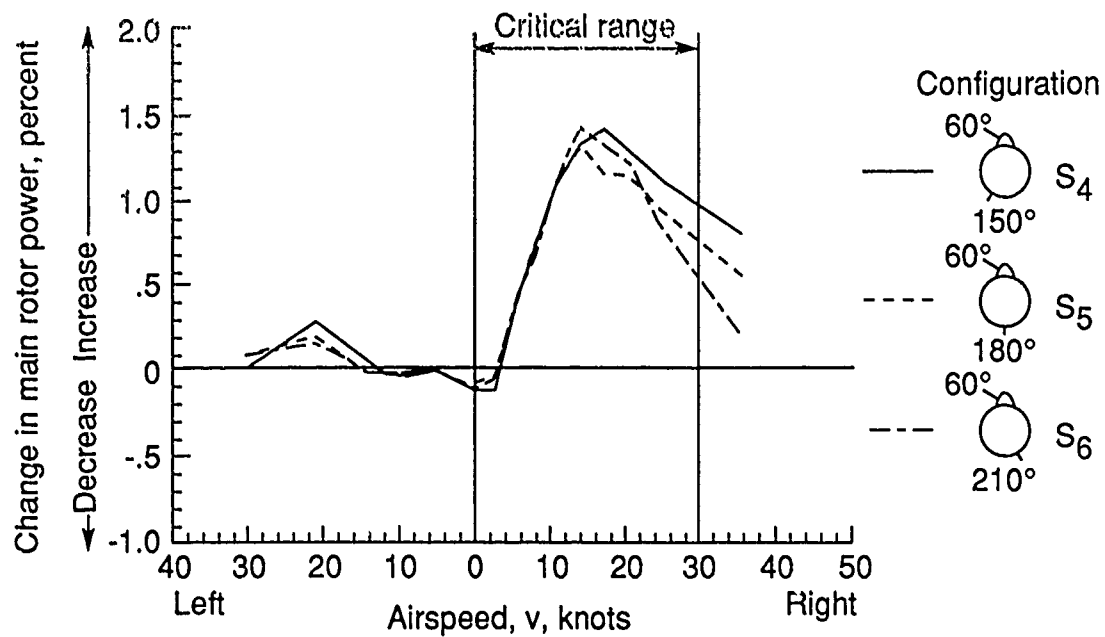
(a) Main rotor power.
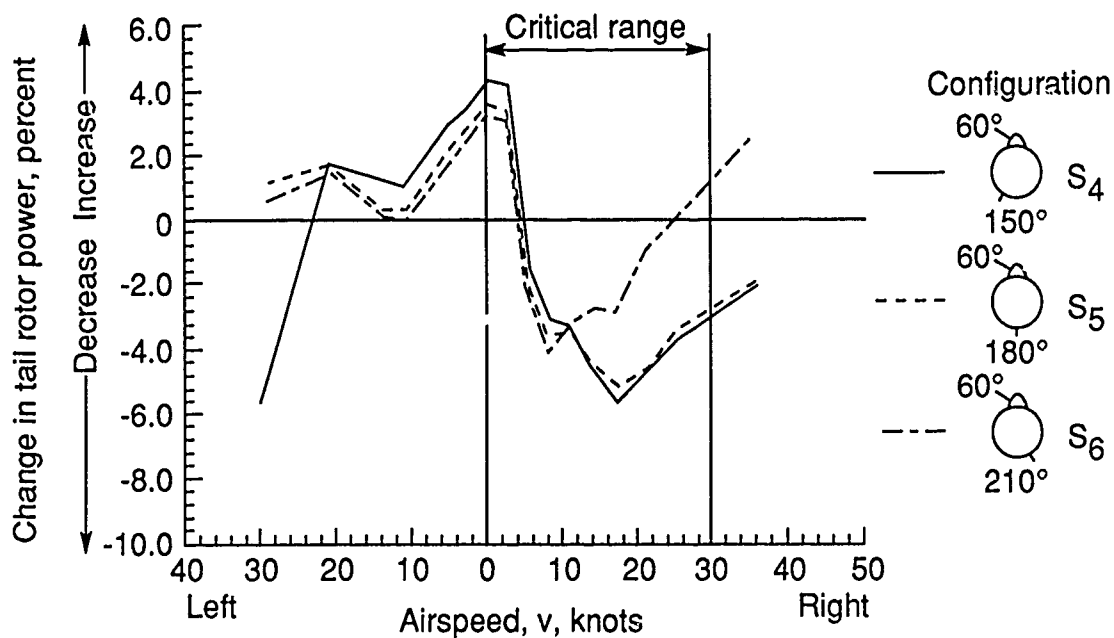
(b) Tail rotor power.

Figure 16. Calculated change in rotor power as function of airspeed for configurations S_4, S_5, and S_6 of OH-58A model.
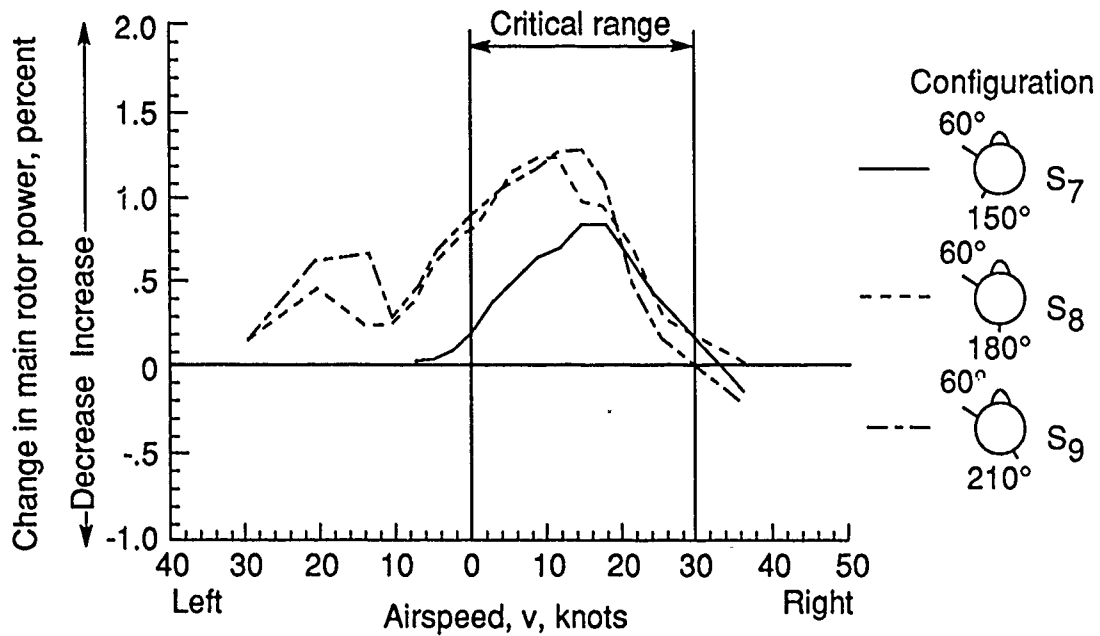
(a) Main rotor power.
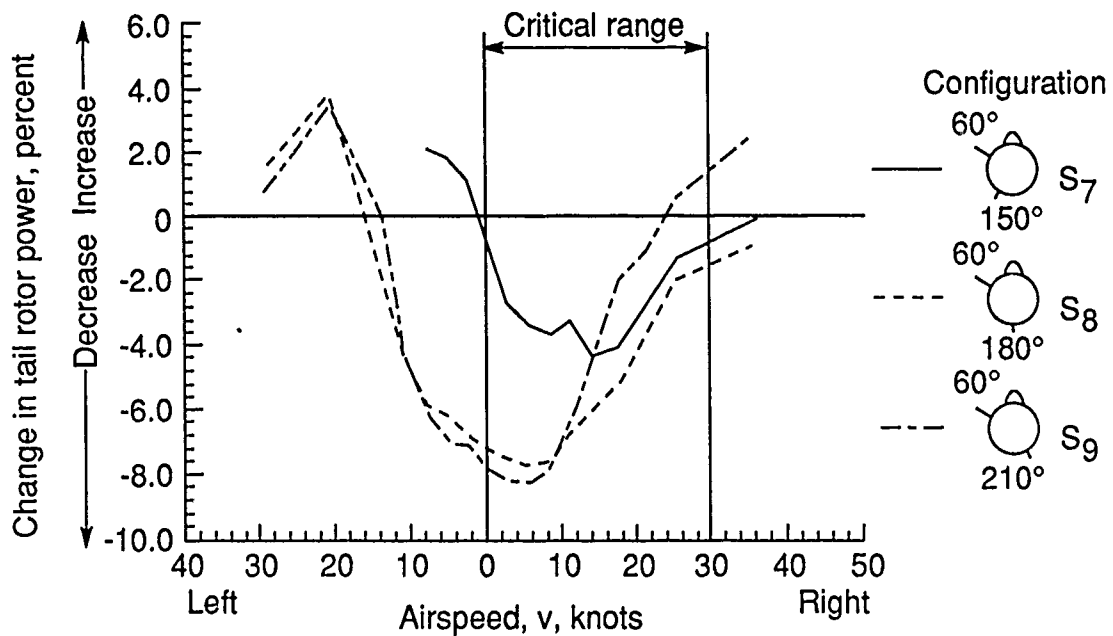
(b) Tail rotor power.

Figure 17. Calculated change in rotor power as function of airspeed for configurations S_7, S_8, and S_9 of OH-58A model.
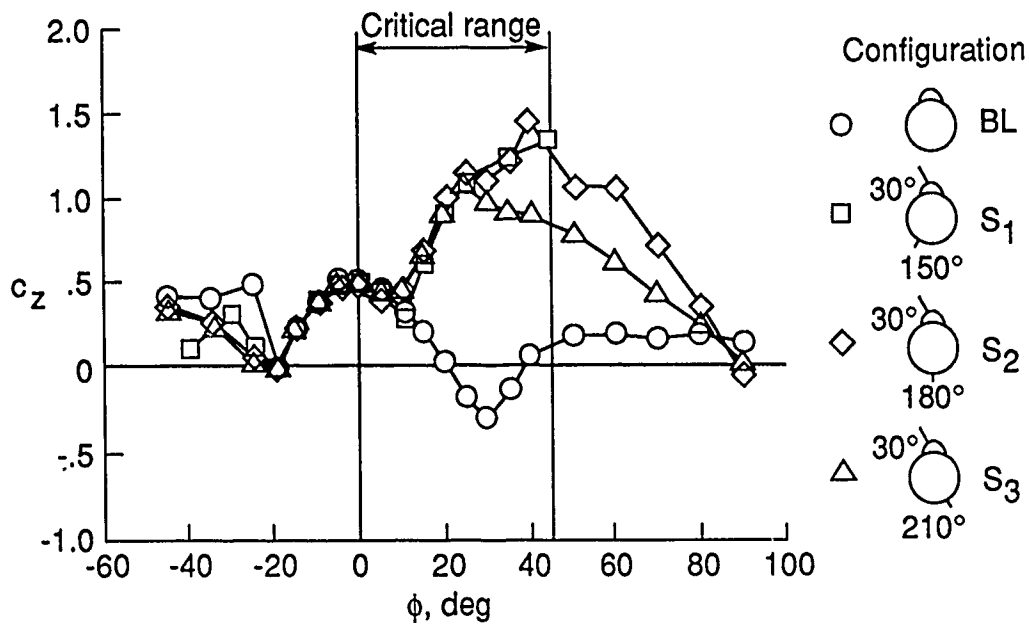
(a) Normal-force coefficient.
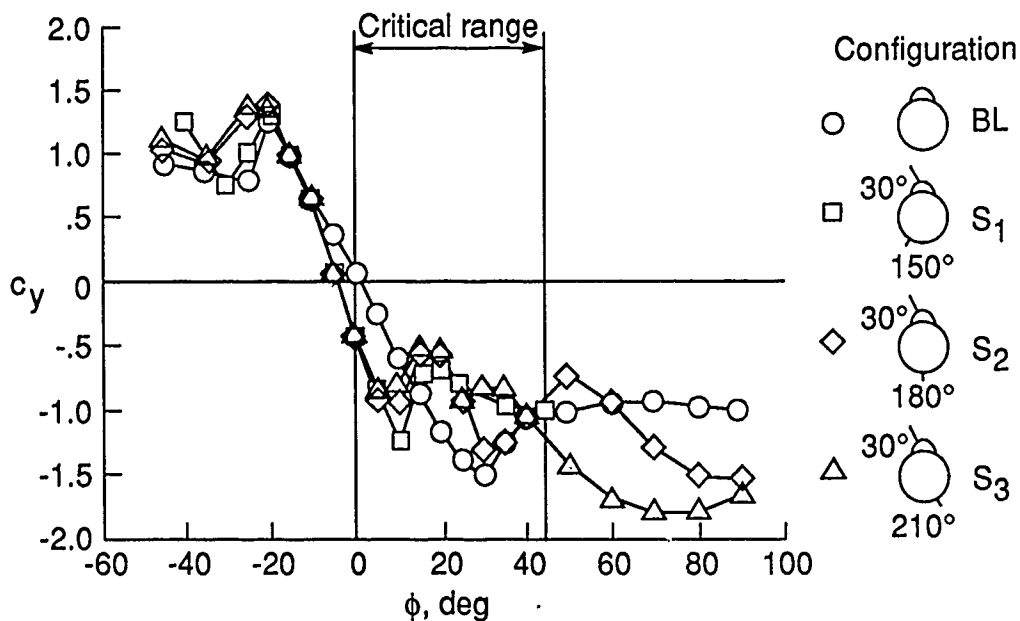
(b) Side-force coefficient.

Figure 18. Effect of flow incidence on c_z and c_y for OH-58D shape and configurations S_1, S_2, and S_3.
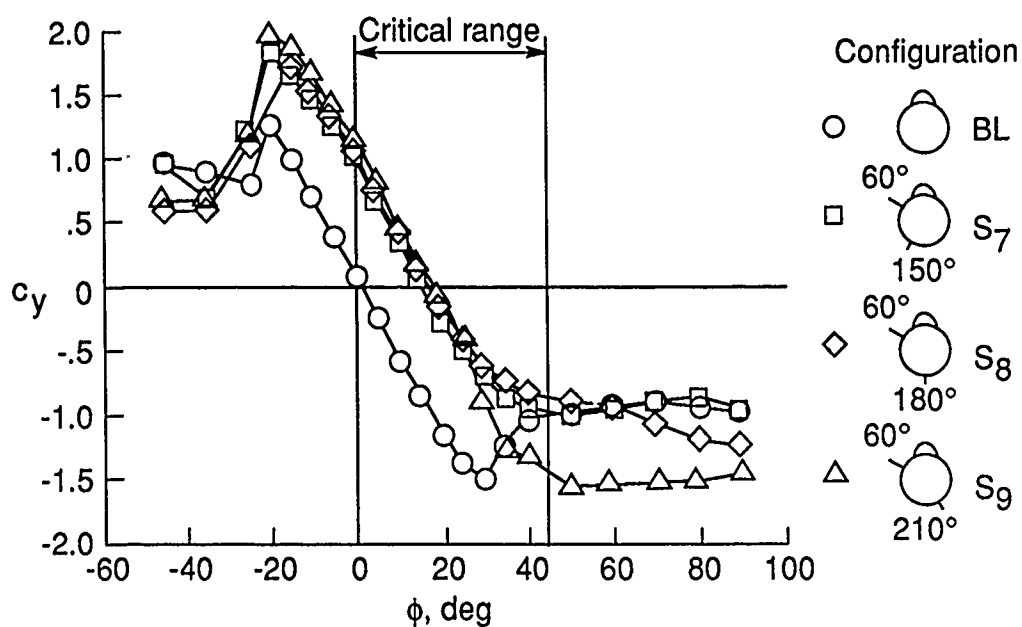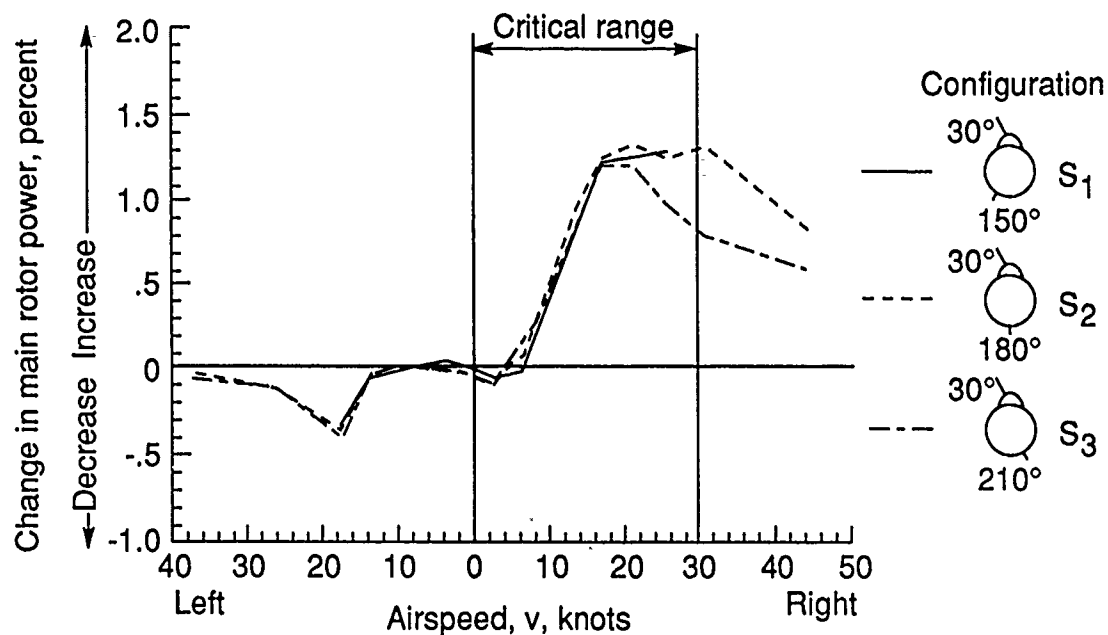
(a) Normal-force coefficient.

(b) Side-force coefficient.

Figure 19. Effect of flow incidence on c_z and c_y for OH-58D shape and configurations S_4, S_5, and S_6.
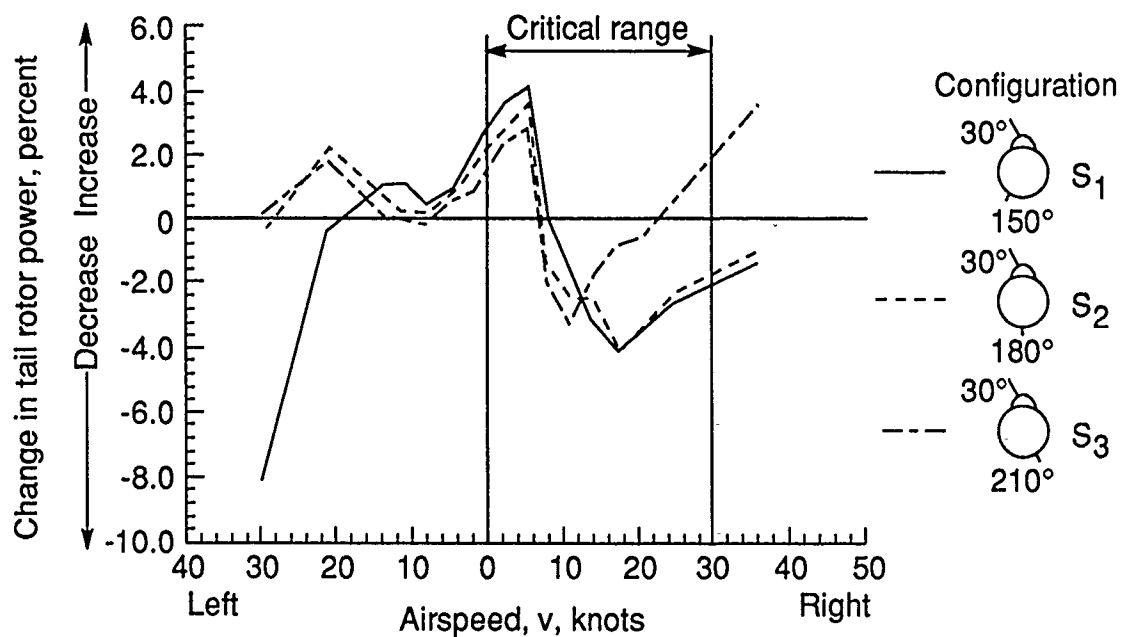
(a) Normal-force coefficient.

(b) Side-force coefficient.

Figure 20. Effect of flow incidence on c_z and c_y for OH-58D shape and configurations S_7, S_8, and S_9.
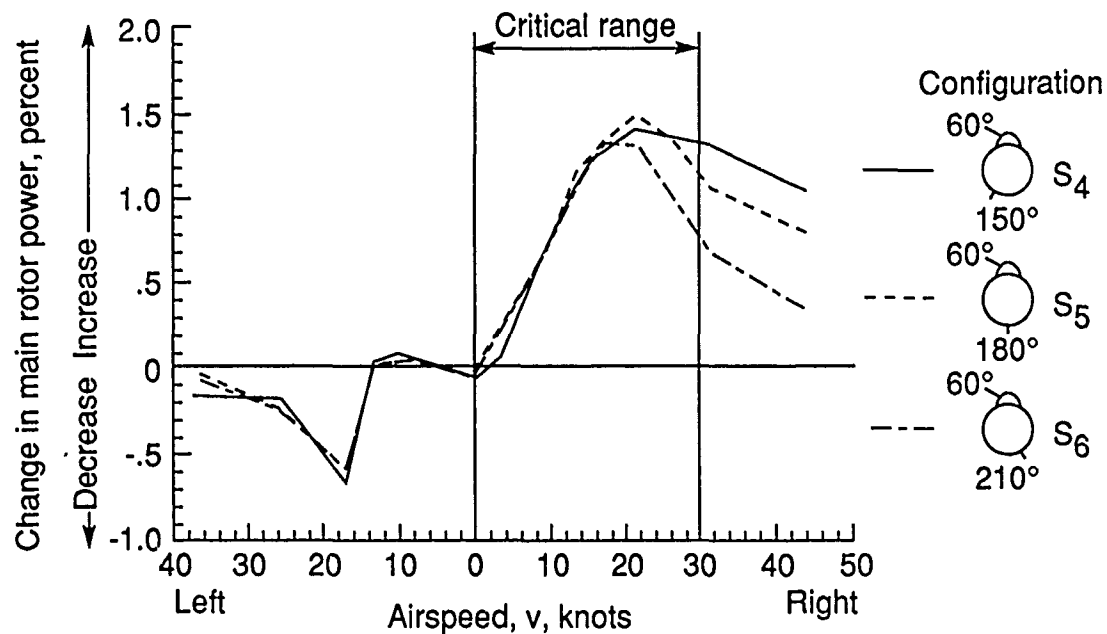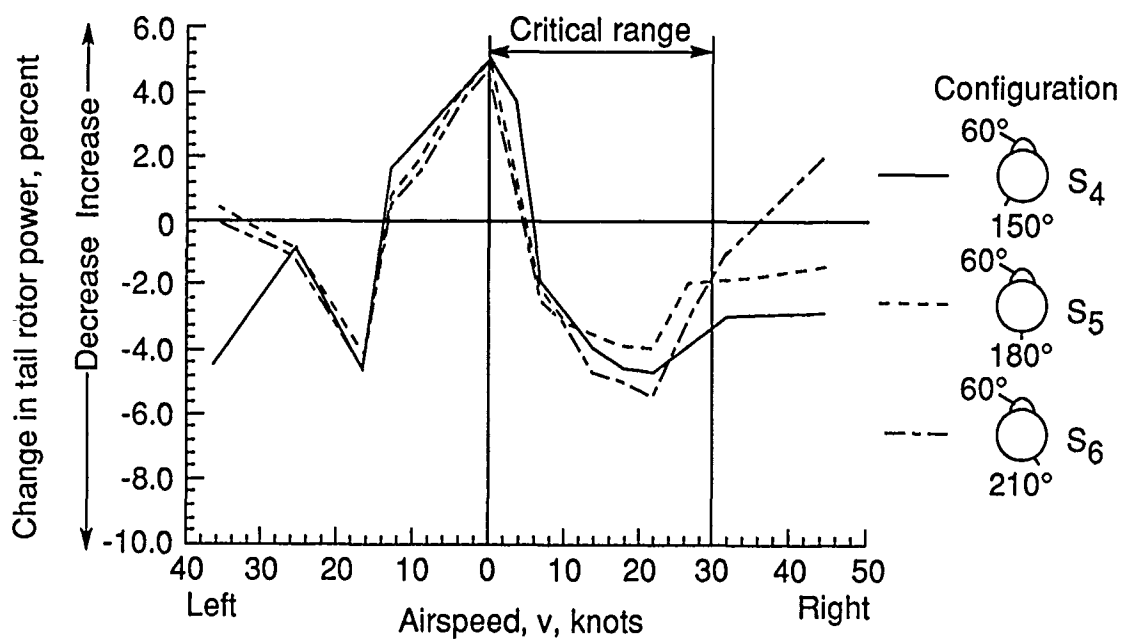
(a) Main rotor power.

(b) Tail rotor power.

Figure 21. Calculated change in rotor power as function of airspeed for configurations S_1, S_2, and S_3 of OH-58D model.

(a) Main rotor power.

(b) Tail rotor power.

Figure 22. Calculated change in rotor power as f.   ·tion of airspeed for configurations S_4, S_5, and S_6 of OH-58D model.
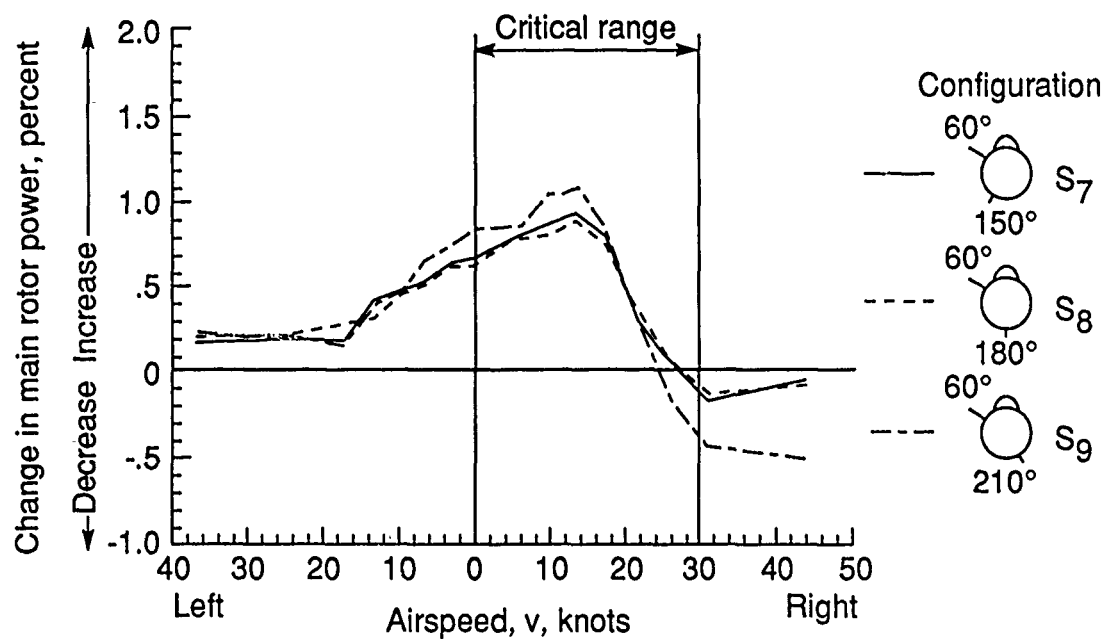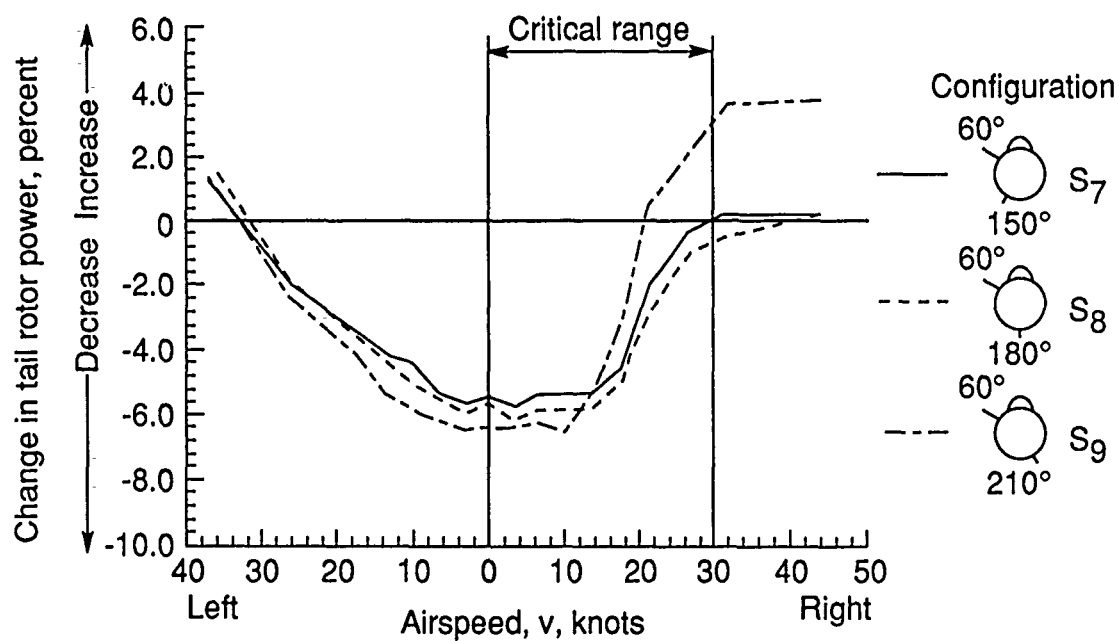
(a) Main rotor power.

(b) Tail rotor power.

Figure 23. Calculated change in rotor power as function of airspeed for configurations S_7, S_8, and S_9 of OH-58D model.

Report Documentation Page

1. Report No. NASA TM-4248 AVSCOM TR-90-B-010	2. Government Accession No.	3. Recipient's Catalog No.
4. Title and Subtitle Aerodynamic Effect of Strakes on Two-Dimensional Tail Boom Models of OH-58A and OH-58D Helicopters		5. Report Date December 1990
		6. Performing Organization Code
7. Author(s) Cynthia A. Crowell and Henry L. Kelley		8. Performing Organization Report No. L-16842
9. Performing Organization Name and Address Aerostructures Directorate USAARTA-AVSCOM Langley Research Center Hampton, VA 23665-5225		10. Work Unit No. 505-61-51-10
		11. Contract or Grant No.
12. Sponsoring Agency Name and Address National Aeronautics and Space Administration Washington, DC 20546-0001 and U.S. Army Aviation Systems Command St. Louis, MO 63120-1798		13. Type of Report and Period Covered Technical Memorandum
		14. Army Project No. 1L162211A47A

15. Supplementary Notes
Cynthia A. Crowell and Henry L. Kelley: Aerostructures Directorate, USAARTA-AVSCOM.

16. Abstract

During hover, helicopters experience significant aerodynamic forces on the tail boom caused by the wakes of the main and tail rotors and by crosswinds. These effects were investigated in the Langley 14- by 22-Foot Subsonic Tunnel on large-scale two-dimensional tail boom models with cross sections representative of the U.S. Army OH-58A and OH-58D helicopters. The effects of longitudinal strakes attached to the models were also investigated. The results with the strakes installed showed a significant improvement at conditions representative of right sideward flight by reducing the side force on the booms. Calculations indicated a 5- to 6-percent savings in tail rotor power. An increased download on the booms was noted because of the strakes.

17. Key Words (Suggested by Authors(s)) Helicopter Antitorque systems Yaw control Tail boom Strakes	18. Distribution Statement Unclassified—Unlimited Subject Category 02

19. Security Classif. (of this report) Unclassified	20. Security Classif. (of this page) Unclassified	21. No. of Pages 32	22. Price A03